FLEXIBLE NANOCOMPOSITE THIN FILMS FOR ELECTRONIC DEVICES

A Dissertation
Submitted to the Graduate Faculty
of the
North Dakota State University
of Agriculture and Applied Science

By

Meshal Mufleh Alzaid

In Partial Fulfillment of the Requirements
for the Degree of
DOCTOR OF PHILOSOPHY

Major Program:
Materials and Nanotechnology

February 2019

Fargo, North Dakota

North Dakota State University
Graduate School

Title

FLEXIBLE NANOCOMPOSITE THIN FILMS FOR ELECTRONIC DEVICES

By

Meshal Mufleh Alzaid

The Supervisory Committee certifies that this ***disquisition*** complies with North Dakota State University's regulations and meets the accepted standards for the degree of

DOCTOR OF PHILOSOPHY

SUPERVISORY COMMITTEE:

Erik K. Hobbie
Chair

Yongki Choi

Orven Swenson

Xiangfa Wu

Approved:

03/15/2019
Date

Erik K. Hobbie
Department Chair

ABSTRACT

Electronic technology is moving towards flexible, durable, and smaller devices with multifunctional capability. To accelerate this movement, creating materials with outstanding properties is critical. Nanocomposites based on single wall carbon nanotubes (SWCNTs) have received considerable attention because of their unique mechanical and electrical properties. When SWCNTs are formed as a sheet, they provide large contact area and ease of control, especially when incorporated into a flexible format. However, when SWCNT films are adhered to an elastic substrate, there are challenges with their use in flexible electronics, such as a reduction Young's modulus under deformation. SWCNT films can undergo plastic behavior at even a small strain because individual SWCNTs slide past each other in response to deformation. To address these challenges, a strain-induced elastic buckling instability for mechanical measurements (SIEBIMM) method was used to query SWCNT film mechanics. The buckling wavelength and the film thickness are two main factors that influence the mechanics of nanocomposite thin films adhered to elastomeric substrates.

SWCNT films coated with a second nanomaterial, such as a polymer thin film or nanocrystals (NCs), have shown a significant enhancement in elasticity. The studies described in this dissertation demonstrate that polymer thin film can reduce the strain softening of SWCNT films, where both yield strain and Young's modulus increase with the introduction of SWCNT-polymer layers. Specifically, the films started to exhibit a strong synergy between SWCNT and polymer at a film thickness of around 20 nm, which is attributed to the thickness approaching the characteristic interfacial width between the two materials. Both a 'passive' polymer thin film (for example, polystyrene-PS) and an 'active' polymer thin film, the conducting polymer poly(3,4-

ethylenedioxythiophene)-poly(styrenesulfonate)(PEDOT:PSS), were investigated, spanning a bilayer to the bulk limit of SWCNT-polymer multilayers.

In addition, ultrathin SWCNT films coated with colloidal NCs have also been investigated. We have utilized two approaches to coat SWCNT films with NCs: Langmuir-Blodgett (LB) and spray coating. Both Si and CdSe nanocrystals showed a roughly two-fold enhancement in film elasticity, which was attributed to an excluded volume effect that prevents the SWCNT rearrangement under an applied strain.

ACKNOWLEDGMENTS

First of all, I would like to thank Prof. Erik Hobbie for his great support. He has smoothed every challenge in my research by guiding me to the right answer. His quick response and answer to my inquiries enable me to achieve the most important goal in my life so far. I would also like to thank my committee members for their guidance and support.

In addition, I would like to thank all my colleagues, with whom I have enjoyed talking and discussing many topics; Eid Almutairi, Matthew Semler, Samuel Brown, Amal Altayyar, Salim Thomas, Tim Twohig, Theresa Elder, Myungkeun Oh and Lina Alhalhooly, as well as all the other MNT faculty and students. Lastly, I would like to thank my dear friends and family for their support.

DEDICATION

This dissertation is dedicated to my lovely wife and little daughter.

TABLE OF CONTENTS

LIST OF FIGURES

LIST OF APPENDIX TABLES

1. INTRODUCTION TO NANOMATERIALS AND NANOCOMPOSITES

1.1. The Definition of Nanotechnology

Nanotechnology corresponds to the size of technological materials being reduced to the scale of nanometers, causing material properties to be altered. Put simply, "nanotechnology" refers to the control and understanding of matter at dimensions between 1 and 100 nm, which can lead to novel properties and applications. A nanometer is one billionth of a meter, which means a sheet of paper is about 100,000 nm in thickness [1]. Figure 1.1 shows the size and scale of nanomaterials.

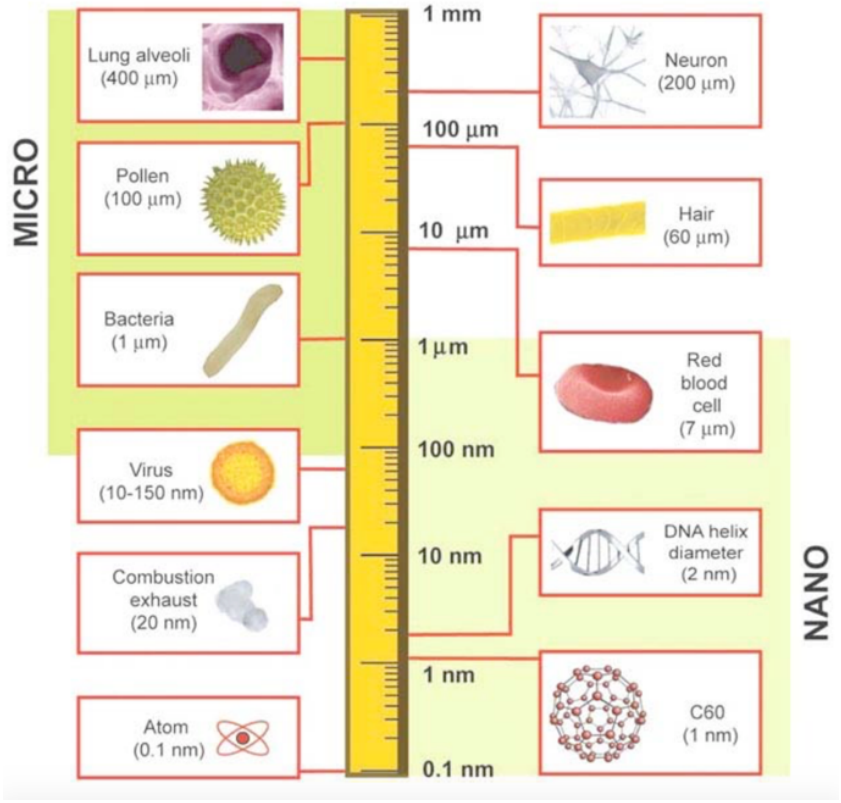

Figure 1.1. Nanomaterial size and scale in comparison to bulk materials [1].

Richard Feynman was the first one who introduced the idea of nanotechnology to the public in 1959 through his lecture "There's Plenty of Room at the Bottom". In this lecture, Feynman described how scientists might control matter at an atomic level. In 1981, a part of his

dream came true with the discovery of the Scanning Tunneling Microscope (STM) with nanoscale resolution [2-3].

"Nanoscale material" is an alternative term for nanomaterial, which can be distinguished from bulk materials. In general, nanomaterials are divided into four groups: zero dimensional nanoscale structures (particulate like shape), one-dimensional nanoscale structures (fiber-like shape), two-dimensional nanoscale materials (sheet-like shape) and three-dimensional nanoscale structure (3D network) [2]. How nanomaterials impact science, technology, and the environment is a principle concern for nanotechnology research.

To understand the implications of nanoscale materials, suppose that we have a mid-size cube of gold. If we are able to bisect the bulk gold in all 3 dimensions, it would exhibit the same intrinsic properties until we reach the nanoscale, where quantum effects would start to emerge. At this nanoscale level, the material's properties – including such things as color, melting point, and interparticle forces – would change. Additionally, the structure of nanomaterials provides high surface to volume and in some instances high aspect ratio, which makes them suitable for many applications including nanocomposites [4].

In addition, the electronic properties of materials have the potential to be influenced by the wave-like properties of electrons inside a material at the nanoscale, which can lead to alteration of the electrical and optical properties. For example, reducing the size of semiconductors to the quantum confinement level (typically below 10 nm) will introduce new optical properties, such as efficient photoluminescence, that have no analogue in bulk semiconductors [3-4].

1.2. Composites and Nanocomposites

Generally, solids are divided into several groups, such as polymers, ceramics, semiconductors, and metals. This classification is based on the chemical and atomic structure. However, composites are formed when two or more of these groups are combined together. In composites, one material is typically a reinforcing phase that could be particles, fibers, or sheets. These are embedded into the base material, which is called the matrix phase. The reinforcing agents provide strength to the matrix associated with low density. Therefore, the combination is stronger, tougher and lighter than individual materials [2-4].

However, when the composite materials have at least one phase at a nanoscale level, nanocomposites are formed. Due to the power of nanoscale materials, the properties of the composites will be maximized, and new properties can emerge. In addition, cost effectiveness in industry is important, and just a small fraction of nanoscale “fillers” can be enough to change the material properties. Lately, nanocomposites containing both organic and inorganic phases have received tremendous attention. The properties of nanocomposites depend not only on the properties of the individual components, but also on the degree of attraction or compatibility between the two phases, which means the bonding and interfacial characteristics between two materials are important and critical [7-8].

However, Toyota has started commercially using nanocomposites in automotive applications in the form of polymer/clay auto parts. Since their introduction, there has been growing attention directed toward nanocomposites with promising potential applications. One of the most important applications is electronics, where nanocomposites in the form of thin films can improve and enhance the electrical properties of materials [2,4].

1.3. The Applications of Nanocomposites in Flexible Electronics

Four decades ago, the thickness of crystalline silicon solar cells was reduced, and they became more flexible for aerospace applications. Today, integrated circuits based on silicon are thinner and more flexible, so smart cards remain active and resist breakage in response to applied strain. The precise meaning of "flexibility" can carry many definitions: elasticity, lightweight, roll-to-roll manufacturability, and stretchability. On the industrial side, flexible electronics means flexible displays and flexible sensors, particularly for biomedical applications. In the research field, researchers have investigated conformally shaped displays, wearable electronics, and skin sensors [9]. Reducing the material thickness to micrometers makes them flexible but sometimes reduces other properties such as crystallinity and electron mobility. Therefore, in some instances the device's conductivity has the potential to be negatively affected.

To overcome such negative effects, nanocomposites open new possibilities for simultaneously enhancing both mechanical and electrical properties. For example, embedding silver nanowires (AgNWs) into a nonconductive polymer enhances the electron mobility through the matrix while the device remains light, flexible and cheap. Combing the conductivity of AgNWs and the flexibility of plastics can improve the conductivity of flexible electronics, but this can only be achieved when nanomaterials are used in the composites [9-11].

The main applications of nanocomposites in flexible electronics are as transparent conductive electrodes (TCEs), active layers in solar cells, and light emitting diodes (LEDs). TCEs and solar cell applications will be discussed in the following sections, 1.3.1 to 1.3.2.

1.3.1. Transparent Conductive Electrodes (TCEs)

Transparent conductive electrodes play a crucial role in optoelectronic devices such as light emitting diodes (LEDs), touch screens, and solar cells. TCEs work as windows for

optoelectronic devices by allowing light to enter or leave the device. Additionally, TCEs work to extract either electrons or holes from the active area of the circuit. Indium Tin Oxide (ITO) is commonly used in TCEs due to its high transparency and low sheet resistance. However, ITO is not abundant and is brittle. Therefore, ITO does not meet the requirements for a new generation of electronics designed to operate normally under deformation.

To replace ITO, alternative materials are required that can meet the same standards while accommodating new platforms. These alternative materials should be transparent and conductive as well as flexible. Several materials have been studied to replace ITO, such as conductive polymers, carbon nanotubes (CNTs), and metal nanowires. However, these materials still show some limitations for ITO replacement. For example, conductive polymers are negatively affected by moisture and radiation, such as degradation in response to UV light exposure [10].

Instead of using individual materials, combining two nanomaterials together to form nanocomposites has shown promise in this regard. For example, coating conductive polymers with nanomaterials such as single-wall carbon nanotubes (SWCNTs) enhances the electrical properties of the polymers while protecting the polymer films from environmental damage. In addition, the device remains flexible, transparent, and conductive [10-11].

1.3.2. Solar Cells

Solar cells are photodiode devices that convert solar energy into electrical energy. The main component of a solar cell is the p-n junction, which is formed when p-type and n-type semiconductors are brought together. A solar cell or photovoltaic (PV) cell is the basic unit in a PV system. Today, most are made with Si, which needs to be purified and doped in order to use it in PV cells. The purification step is a major factor that makes such PV systems expensive [9].

In the purification step, the top of a Si wafer is doped with a material such as phosphorus with an excess of electrons, which makes a thin layer of n-type semiconductor. However, the base side of the Si wafer is doped with a different material, such as boron, that has an excess of holes. Thus, this forms a p-type semiconductor in the base. When the p- and n-type materials are brought together, they form a p-n junction, with the electrons travelling to the p-side and the holes going to the n-side until equilibrium is reached. When the solar cell is exposed to sunlight, photons excite electrons in the p-n junction, and the electrodes then pull these electrons and holes out of the cell through a circuit [14]. Figure 1.2 shows the basic elements of a PV cell (right) and the semiconductors commonly used to form either p- or n-type materials in solar cells (left).

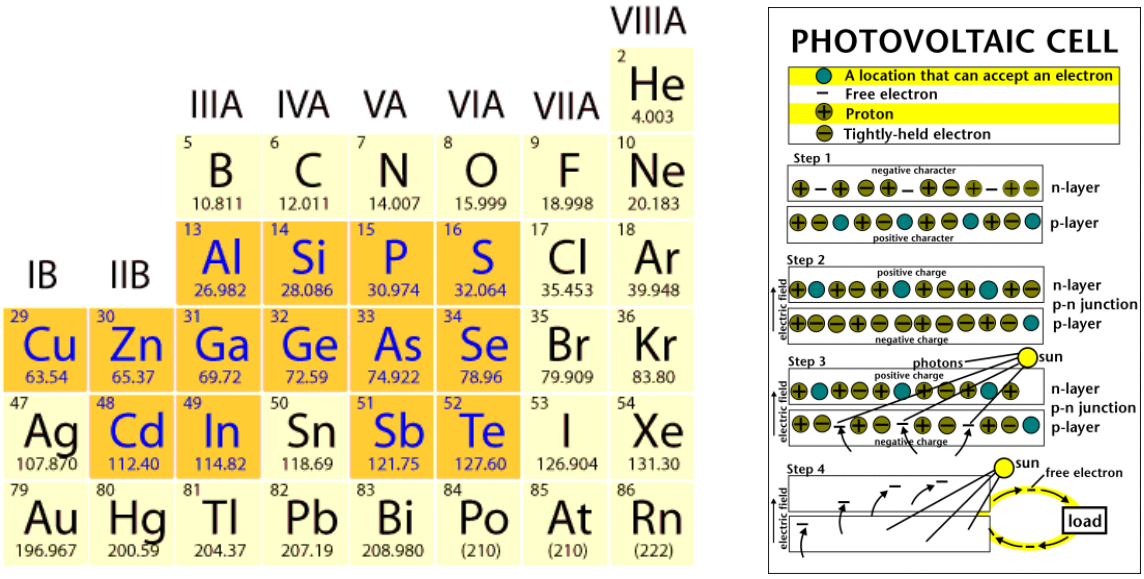

Figure 1.2. Semiconductor groups (left) and the PV cell structure (right) [15].

As mentioned above, purifying Si is very costly. One solution to overcome this is to use thin film solar cells based on nanocomposites, which are the combination of nanomaterials such as nanoparticles or CNTs.

In addition, the band gap will be altered by quantum confinement when the size and shape of an inorganic material are reduced. This also opens new possibilities for choosing the

spectral window or the complementary absorption profile. Additionally, these nanocomposite thin films can be easily deposited by various deposition techniques, such as vacuum filtration, drop casting, spin coating, electrospinning, spray coating, or dip coating. Thus, nanocomposites can be a good replacement for TCEs in PV cells. Figure 1.3 shows the areas that can be improved upon in order to achieve high-efficiency flexible solar cells [10-11].

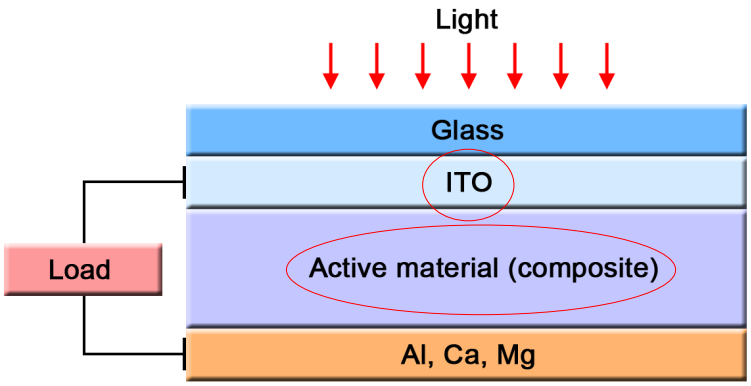

Figure 1.3. Solar cell structure [17].

1.4. Objectives and Approaches

In this dissertation, we mainly focus on the possible replacement of ITO and the concurrent enhancement of thin-film mechanics utilizing nanocomposites. The main materials utilized here are SWCNT thin films, which are then "filled" with other nanomaterials in order to prevent individual SWCNTs from bundling in response to the applied strain. In Chapter two, the properties of nanomaterials that form nanocomposites will be covered in detail. Single wall carbon nanotubes (SWCNTs) and SWCNT thin films will be examined, as well as the potential fillers, such as silicon nanocrystals (SiNCs) and poly(3,4-ethylenedioxthiophene)-poly(styrenesulfonate) (PEDOT:PSS) films. Chapter three covers the experimental procedures and the characterization methods, whereby SWCNT thin films are coated with a second nanomaterial such as NCs or polymer thin films in order to enhance the mechanical properties such as elastic modulus and yield strain. In Chapter four, the rigidity and bulk limit of SWCNT-

polymer multilayer nanocomposites are discussed. Chapter five covers the mechanical enhancement of a conductive polymer layer sandwiched between two SWCNT films. Chapter six covers the elasticity enhancement of ultrathin SWCNT films coated with a monolayer of CdSe NCs, while Chapter seven covers SWCNT films coated with SiNCs using a different deposition technique. Finally, Chapter eight provides a summary and outlook for nanocomposites in the flexible electronics field.

2. THE PROPERTIES OF NANOCOMPOSITE MATERIALS

CNTs have been intensively studied due to their extraordinary electrical, mechanical, and thermal properties. They are promising nanomaterials for many applications, including flexible electronics. In this Chapter, SWCNTs and other nanomaterials such as SiNCs and PEDOT:PSS will be considered. First, the properties of SWCNT and SWCNT thin films will be examined in the following subsection. Then, thin films made from the conductive polymer (PEDOT:PSS) and quantum dots (SiNCs) will be reviewed, where their properties and synthesis methods will be discussed in detail. In addition to our own work, we also include a review of the recent literature on the properties of SWCNT, PEDOT:PSS, and SiNCs.

2.1. Single Wall Carbon Nanotubes (SWCNTs) and SWCNT thin films

Carbon, with an atomic number equal to six, is the fourth most abundant element in the universe. In comparison to the other elements, carbon has a number of unique allotropes. Most notably, carbon nanotubes (CNTs, a high-aspect-ratio cylindrical allotrope), were discovered in 1991 by Sumio Iijima. CNTs are a sheet of graphite “rolled up” into a cylinder [18]. Recently, CNTs have received a large amount of interest focused on a better understanding of their structure and potential applications, specifically the impact of their diameter, length, and chirality. In addition, CNTs can be either single-walled (SWCNTs) or multi-walled (MWCNTs).

In this subsection, SWCNTs will only be considered because the properties of SWCNTs are superior to MWCNTs and SWCNTs are the material studied in this dissertation. SWCNTs can be thought of as “rolled-up” graphene sheets, with diameters that range from 0.3 nm to 3 nm and lengths that can be up to several millimeters. Due to their small diameter and large length, SWCNTs have very high aspect ratio, which makes them appealing for many applications. In addition, SWCNTs can be either metallic or semiconductor, depending on their molecular

symmetry. In other words, they can be conducting or semiconducting depending on how the graphene sheet is "rolled up". Because of this unique attribute, SWCNTs are of interest for numerous applications in microelectronics and flexible electronics [18].

The chiral vector (*n*, *m*) is used to describe the structure of the tube, where *n* and *m* are integers (shown in Figure 2.1). When *n* and *m* are equal, an armchair structure is formed, where the armchair SWCNT is metallic. On the other hand, if *m* is equal to zero, a zig-zag structure is present and the SWCNT is semiconducting [19]. In general, the chirality of SWCNTs determines their electronic properties: metallic vs. semiconducting [19].

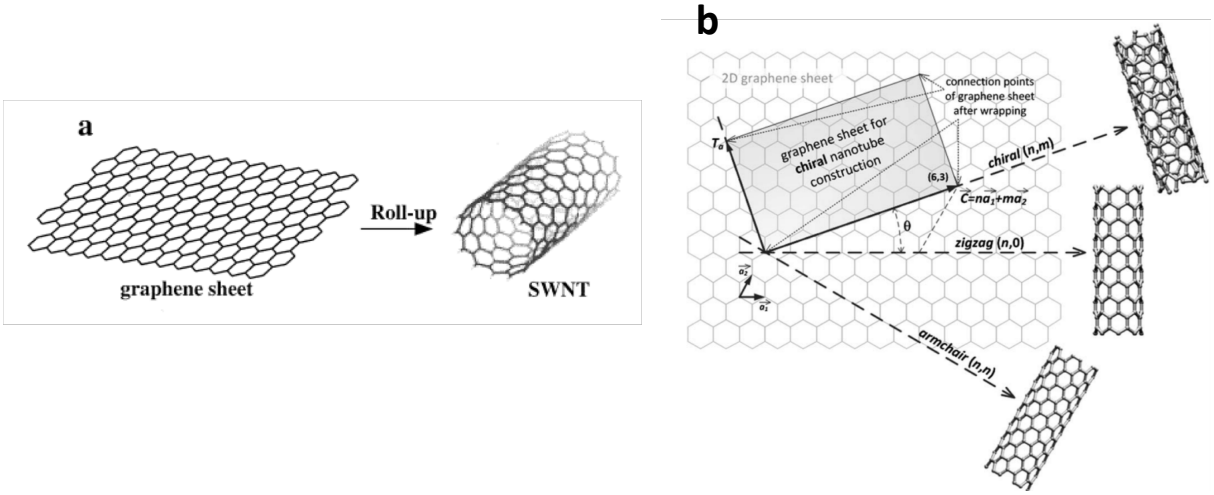

Figure 2.1. SWCNT (a). The chiral vector (*n*, *m*) (b) [19].

In addition, SWCNTs can withstand high current densities due to their strong C-C bonds and they can accommodate high signal frequency (up to 10 GHz) when utilized as interconnects on semiconductor devices, where electron transport occurs along the tube axis [20]. The chirality also plays a very important role in determining the diameter of a SWCNT through $d = \frac{a}{\pi}\sqrt{n^2 + m^2 + nm}$, where *a* is the length of the C-C bond [19].

SWCNTs exhibit high material strength due to the nature of the bond between carbon atoms associated with their unique tube-like structure. In a SWCNT, each C atom is bonded with

three carbon atoms, which forms three sp^2 orbitals through hybridization. For example, to cleave a SWCNT, 10 bonds must be broken with each bond having 2.7 eV bond energy. This bond energy is strong and leads to unique mechanical properties [21].

Theoretically, the Young's modulus of a SWCNT is predicted to approach 1.2 TPa, which is in good agreement with experimental data showing 1.3 TPa for individual SWCNTs deposited on an elastic substrate [22]. The tensile strength, where the material fails under stress, theoretically falls between 150 to 180 GPa for SWCNTs [23]. However, the maximum tensile strength that has been obtained experimentally is 70 GPa, which has been attributed to defects. In addition, SWCNTs have lower density ($\sim 0.8\ \mathrm{g}/cm^3$) in comparison to other materials [19].

To synthesize CNTs, chemical vapor deposition (CVD), arc discharge, and laser ablation are the three main methods. In CVD, a mixture of hydrocarbon gas (C_nH_m) is inserted into an inert chamber in the presence of a metal catalyst. At high temperatures (700-900 ℃), the hydrocarbon gas is decomposed at atmospheric pressure, and both MWCNTs and SWCNTs are formed and deposited on the chamber surface. The second technique is arc discharge. Here, two carbon sources are placed end-to-end in an inert closed chamber at low pressure. These carbon sources are separated by 1 mm. A 20 V potential difference is applied, causing a high temperature discharge between the two sources. This causes one carbon electrode to vaporize. As a result, CNTs and other carbon related materials are deposited on the other electrode. However, this technique requires a further step for purification. The third method is laser ablation in which an intense laser pulse is used to vaporize the carbon target in an inert tube furnace at 1200 ℃. The inert gas passes through the tube to collect the grown nanotubes on a cold surface. This method is used to synthesize SWCNTs in the form of ropes. Figure 2.2 shows schematics of all three methods that are used to produce CNTs [19].

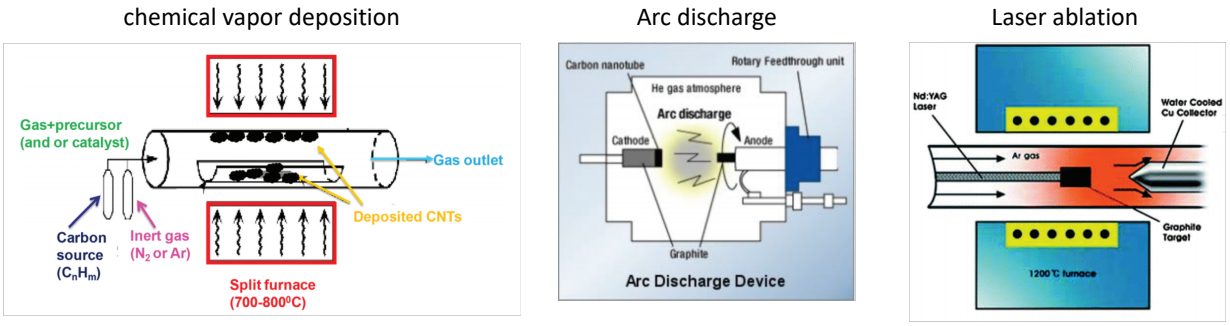

Figure 2.2. CNT synthesis methods [24].

A sheet-like morphology of SWCNTs provides a rather simple structure that can be readily processed and modeled. Intuitively, a layered structure also offers a large interfacial contact area, but without the need to focus on the true state of nanotube dispersion in the matrix, which is not ideal in most practical scenarios. The theoretical properties of SWCNT films have not yet been fully realized, while the unique properties of individual SWCNTs are due to their individual structure. van der Waals interactions are the forces that holds individual SWCNTs together to form a film. This force is weaker than the C-C bond that exists in the individual SWCNT. However, van der Waals forces can also cause the SWCNT network to form bundles and ropes, which will affect the mechanical properties of the film. The strain induced coarsening of these bundles and ropes results in the strain softening of SWCNT films, which means that the Young's modulus will decrease in response to an applied strain, even at a small magnitude [25-26]. In contrast, large scale bending of SWCNT films suspended in a fluid, such as ethanol, can show nearly ideal behavior [27].

In general, a SWCNT thin film is a semi-porous material, as shown in Figure 2.3. SWCNT thin films can be fabricated through many techniques such as spin coating, drop casting, and vacuum filtration. In this dissertation, SWCNT thin films made via vacuum filtration will be discussed.

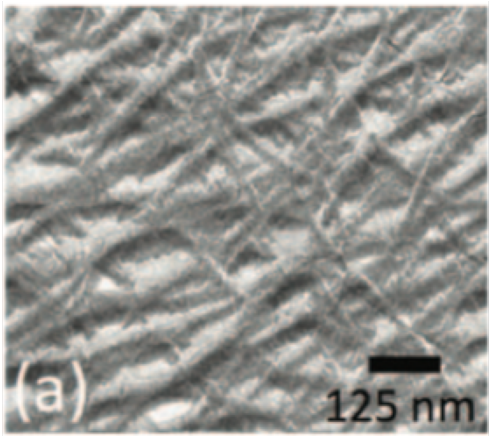

Figure 2.3. TEM image of a SWCNT film produce via vacuum filtration [28].

The attraction between SWCNTs in a film is not limited to van der Waals interactions. Excluded-volume repulsion and sliding friction are other forces that impact the properties of SWCNT thin films. The effective van der Waals attraction becomes stronger when the diameter of the SWCNT is smaller and their length is longer, which is attributed to the higher electron density in smaller diameter SWCNT [28-29].

In contrast to 1 TPa individual SWCNTs, SWCNT thin films still show a high Young's modulus on the order of 10-100 GPa [28-29]. However, a SWCNT thin film adhered to a soft substrate can show plastic changes in microstructure under a small compressive strain. This is because SWCNTs form bundles through van der Walls interactions between individual nanotubes, which is associated with the small diameter, long length, and high aspect ratio of a typical SWCNT. Once a compressive strain is applied to a SWCNT thin film adhered to an elastic substrate, individual SWCNTs and bundles slide and rearrange, which leads to plastic deformation and a Young's modulus that decreases with increasing strain [25-29].

Extensive work was done by Semler et al on SWCNT thin films capped with polystyrene (PS) thin films for different electronic SWCNT types [28]. In that work, both the Young's

modulus and yield strain of the thinner capped films were enhanced, while thicker films showed a reduction in Young's modulus and an increase in yield strain [25,28]. Therefore, PS fillers reinforced the thinner SWCNT films due to the infiltration of PS into the porous structure, while they acted as plasticizers for thicker films [28]. Figure 2.4 shows the relationship between Young's modulus and film thickness for different electronic type for both capped and uncapped SWCNT films [28].

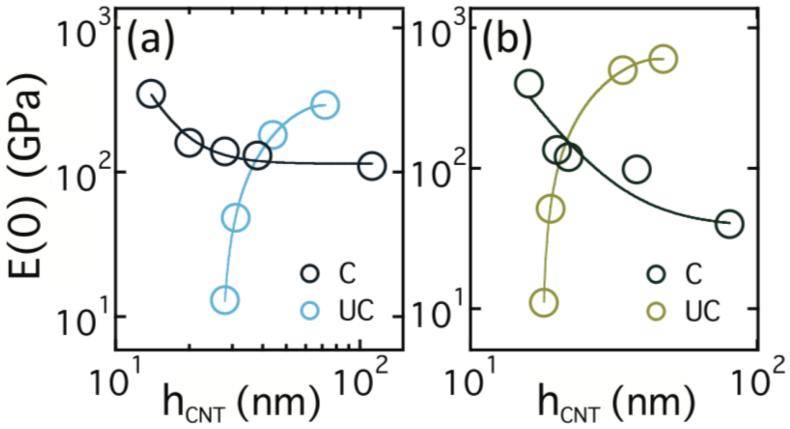

Figure 2.4. Zero-strain modulus vs. film thickness for metallic SWCNT films (a) and semiconducting SWCNT films (b), both pristine (UC) and capped (C) with a think polymer layer [28].

In addition to their mechanical properties, the electrical properties of SWCNT films can be negatively affected when they are subjected to an applied strain. This is due to a reduction in the number of quality SWCNT-SWCNT contacts in response to strain, a situation that can be compounded by residual surfactant. Doped SWCNT thin films exhibit a reasonable resistivity that makes them a suitable replacement for ITO, but they are still less conductive in comparison to individual SWCNTs. This is due to the relatively large contact resistance associated with a CNT-CNT junction [25-28]. Figure 2.5 shows the sheet resistance of thin SWCNT films, both with and without chemical doping.

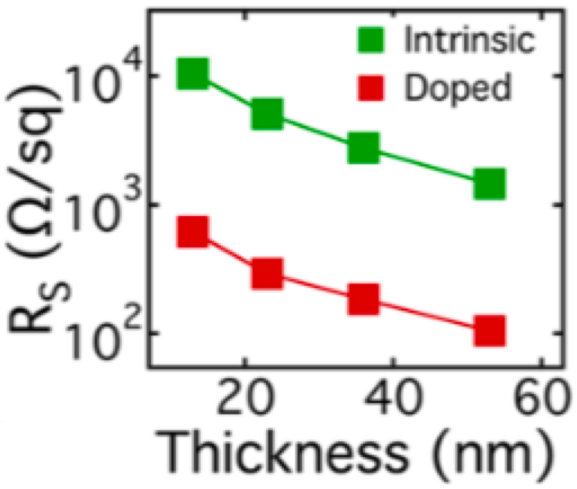

Figure 2.5. The sheet resistance of SWCNT films for a variety of film thickness, both with and without chemical doping. Reprinted with permission from Ref. [27]. Copyright 2019 American Chemical Society.

2.2. Poly(3,4-ethylenedioxthiophene)-poly(styrenesulfonate) (PEDOT:PSS) thin films

Conjugated polymers can compete with inorganic materials for conductivity. In addition, polymers are flexible and tough. Combining these two features, conductivity and flexibility, is key for new applications in flexible electronics. One of these polymers has gained much recent attention: Poly(3,4-ethylenedioxythiophene) poly(styrenesulfonate) (PEDOT:PSS). PEDOT:PSS is a macromolecular salt of two monomers, PEDOT and PSS. PEDOT (3,4-ethylenedioxythiophene) is a conjugated polymer and carries positive charges, and PSS (sodium polystyrene sulfonate) carries negative charges, with the chemical structure of each shown in Figure 2.6. PEDOT:PSS can be manufactured at a large scale. The main approaches that are commonly used to fabricate PEDOT:PSS thin films include vacuum filtration, wet spinning, drop casting and spin coating [30, 31].

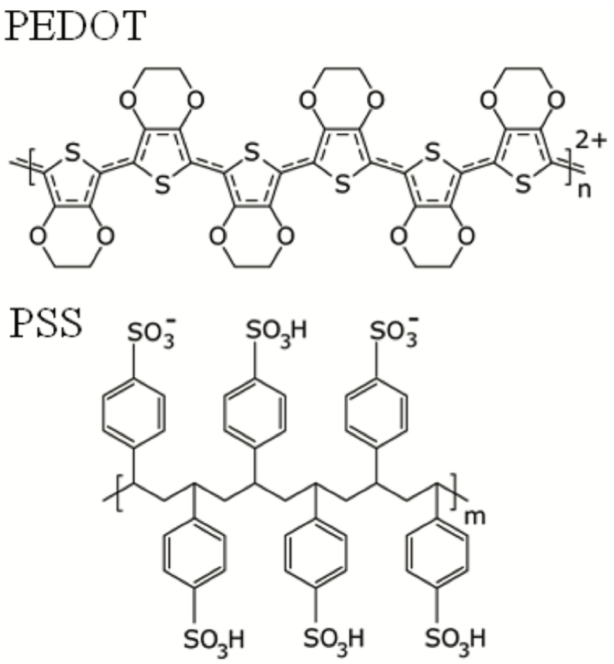

Figure 2.6. Chemical structure of PEDOT:PSS [31].

The PEDOT:PSS is a conductive, transparent polymer. In addition, it is a ductile mixture that can be shaped easily. Good electrical conductivity is the most attractive PEDOT:PSS property and this makes it a suitable choice for use as transparent electrodes in OLEDs, touch screens, or electronic paper [32]. However, factors that affect the quality of films include 1) the viscosity of the complex, 2) adhesion between the film and the substrate, and 3) the surface tension of the film [33]. All these factors can be controlled by using different grades of PEDOT:PSS, which can be done by tuning the solid content in the complex, the ratio of PEDOT to PSS, the gel-particle dispersion state, or by adding additives, such as surfactants, binders or cross-linking agents. Another feature of the complex is its thermal stability. To remove water, the complex has to be heated and baked [33]. Thin films, for example, are dried by heating them on a hot plate to temperatures above 100 ℃ and annealing them there for several seconds. Drying can also be initiated by applying vacuum or using infrared (IR) radiation. PEDOT:PSS can be thermally stable up to temperatures of 200 ℃ [33]. However, PEDOT:PSS can degrade and be

affected by ultraviolet light and water, so isolating the PEDOT:PSS film from moisture is essential for film durability [33].

Recently, the mechanical properties of PEDOT:PSS thin films have been studied extensively. The theoretical Young's modulus for each constituent polymer is predicated to be 3.5 GPa [34]. Thus, PEDOT:PSS films should have the same or even higher modulus according to polyelectrolyte multilayer (PEM) theory [34-36]. In composite theory, the Young's modulus of the composite is theoretically 2-3 times higher than the parent polymer due to strong ionic bonding or electrostatic cross-linking between the layers [34]. Tahk, et al. experimentally found the Young's modulus for PEDOT:PSS films to be 2.3 GPa, and they attributed the lower modulus to a weak ionic bond and a low ratio of PEDOT to the long PSS chain in the PEDOT:PSS films [34]. However, other work has shown 2.5-to-3 GPa for the Young's modulus when the tensile test was done on thick PEDOT:PSS films, which is in good agreement with a composite theory where PEDOT prevents the system from achieving full cross-linking [37].

Due to the conductivity of PEDOT:PSS thin films, this material has been used and investigated widely to replace current electrodes based on indium tin oxide, or ITO. PEDOT:PSS is more flexible and is more abundant [37-38]. From the literature, the conductivity of PEDOT:PSS can be up to 4600 (S/m), and transparent conductive electrodes require conductivity higher than 1000 (S/m) [32]. Figure 2.7 shows an example of PEDOT:PSS conductivity for a variety of film thicknesses.

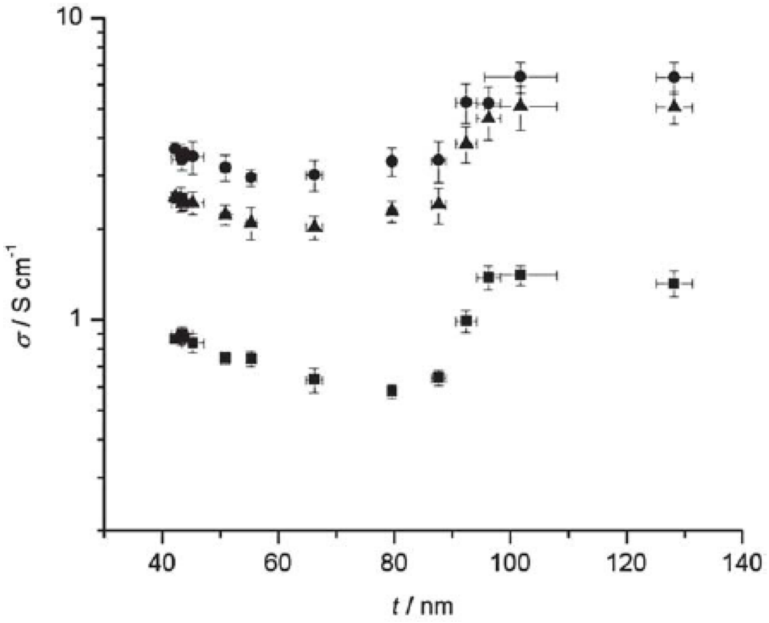

Figure 2.7. The conductivity of PEDOT:PSS for a variety of film thicknesses [38].

The conductivity of PEDOT:PSS films shows a slight reduction for films thicker than 40 nm and thinner than 90 nm, while films higher than 90 nm show an improvement in conductivity [38]. Greco, et al. attributed this change in conductivity to the nature of the electronic pathways [38]. The conductivity pathway is almost straight, where PEDOT forms a pancake-like shape inside the PSS chain. Increasing the film's thickness leads to the conductive PEDOT staking together. For thicker films, the PEDOT forms at least two parallel paths so the electrons can pass easily, as illustrated in Figure 2.8 [38].

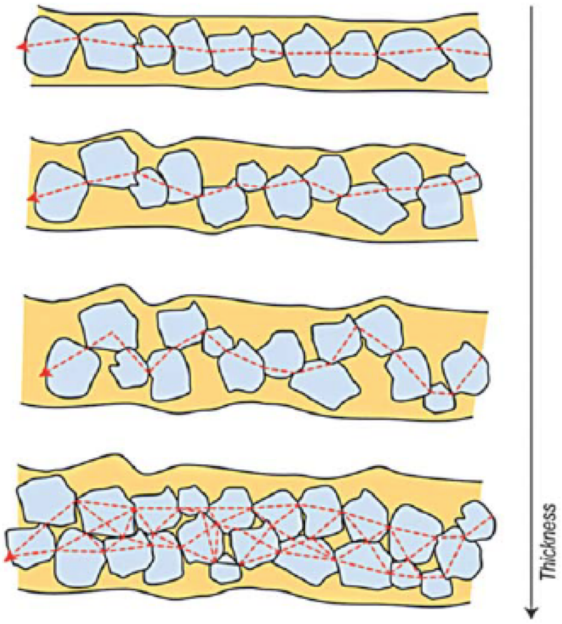

Figure 2.8. Conductivity path as function of PEDOT:PSS film thickness [38].

2.3. Silicon Nanocrystals (SiNCs)

Generally, material properties become altered when the particle size approaches the nanoscale. Because of this, nanomaterials are targeted for potential opportunities covering a wide range of applications, such as LEDs and solar cells. Currently, bulk silicon still dominates the electronics market [39].

Over the past several years, silicon nanocrystals (SiNCs) have received considerable research attention due in part to their low toxicity in comparison to other quantum dots, such as CdSe nanocrystals [40]. Desirable photoluminescence and other optical properties can be achieved when the size of Si materials is reduced below the exciton Bohr radius, or ~ 4.5 nm [41]. Specifically, the band gap energy can be increased by decreasing the SiNC size, making it possible to shift the bandgap energy in the vicinity of the optimum energy gap (i.e. 1.12 eV) and enhance the photoluminescence quantum yield [40-42]. A reasonably strong photoluminescence in the visible-to-red region of the spectrum can be achieved [42]. Additionally, multiple-exciton

generation in SiNCs is another property that has been widely investigated for utilizing SiNCs in solar cells [42-44]. An exciton with energy much larger than the bandgap energy (at least twice) has an increased probability of splitting into multiple excitons instead of losing its excess energy in the form of heat and relaxing to the band edge. If extracted successfully from the dot, these multiple excitons have the potential to lead to a higher photocurrent in the solar cell, or if the excitons recombine radiatively, an enhancement in photoluminescence efficiency [42-44].

Recently, reasonably high conversion efficiency has been demonstrated in a new generation of solar cells based on colloidal QDs, such as SiNCs [44]. One platform that recently exploited confinement effects in Si-based nanostructures is inorganic/organic solar cells [42]. There are two potential reasons for using SiNCs in hybrid solar cells: 1) light-harvesting improvement by broadening the region of the solar spectrum over which light is absorbed by using different sizes of SiNCs, and 2) the extension of device lifetime by replacing organic molecules with more stable inorganic dots [26,42].

The synthetic methods used also play an important role in determining SiNC optical and electrical properties [44]. For instance, using a non-thermal plasma method to produce the SiNCs leads to nanocrystals with a diameter of 3-4 nm and photoluminescence in the red region (600-800 nm) of the visible spectrum [45]. In contrast, blue emitting (400-500 nm wavelength) crystalline Si QDs with a 2-3 nm diameter can be produced through a reverse micelle containing silane [46]. However, using a non-thermal plasma method to synthesize the SiNCs has produced NCs with higher crystallinity, which leads to an improvement in SiNC optical and electronic properties. The non-thermal plasma approach typically utilizes a mixture of silane and argon gas flowing through a small diameter tube under low pressure. The quartz tube is surrounded by two electrodes and is powered by a radio source [45,83]. The plasma that forms when the gas mixture

passes through the quartz tube leads to nanoparticle nucleation and growth. The nanoparticles (NPs) are collected through a filter and then dispersed in an organic solvent for passivation. Generally, the size of the NPs can be controlled by regulating the gas-flow rate [43,45]. Figure 2.9 shows the schematic of nonthermal plasma for SiNC production.

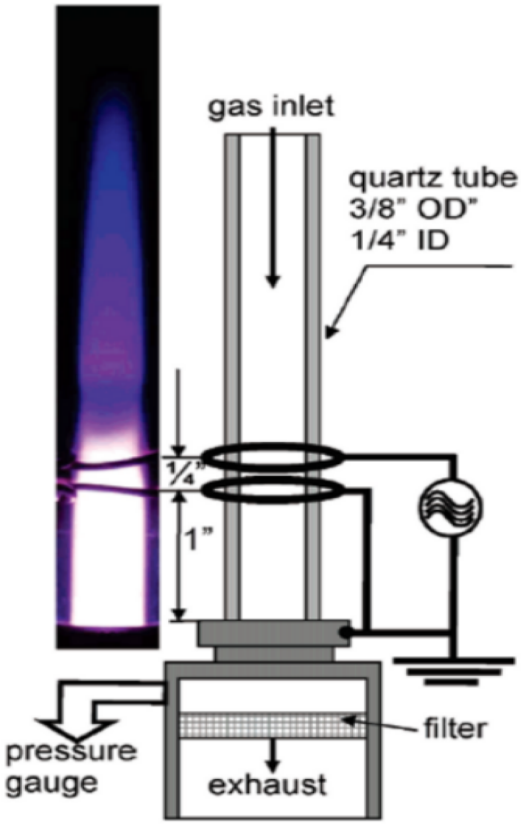

Figure 2.9. Non-thermal plasma for SiNC production. Reprinted with permission from Ref. [45]. Copyright 2019 American Chemical Society.

Bulk Si material has been used extensively in electronics applications over other semiconductors. However, bulk Si is not suitable for photonic devices due to its very limited radiative efficiency and indirect energy gap, as shown in Figure 2.10 [43].

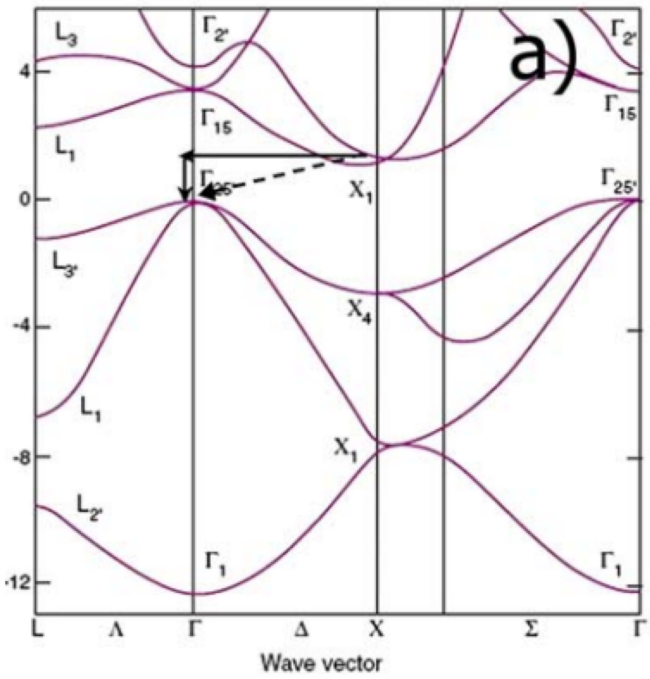

Figure 2.10. Band structure of bulk Si [43].

For indirect band-gap material, the valence band is filled completely with electrons while the conduction band is empty at zero degrees Kelvin, and the bands are separated by a region of forbidden energy (the band gap). As mentioned above, Si has an indirect band gap, where the maximum of the valence band and the minimum of the conduction band are not aligned in *k*-space. The valence band has a maximum peak at the Brillouin zone center (Γ point), while the minimum of the conduction band is close to the X point [43].

Due to the limitations of bulk Si with respect to the absorption of photons with energy less than the band gap, improvements in device efficiency require new approaches. Moreover, the band gap value of bulk Si implies that the interaction with the visible spectrum has limitations [42-43]. Adjusting the gap through quantum confinement could help Si find new uses for both electronic and optical applications. Photoluminescence (PL) at room temperature can be observed for Si nanostructures in a porous silicon (p-Si) structure [47]. Consequently, silicon

nanoclusters, silicon quantum dots (Si-QDs) and silicon nanocrystals (SiNCs) have attracted considerable research interest [39-51]. As shown in Figure 2.11, shrinking SiNC size increases the band gap energy due to quantum confinement, leading to the emission of different colors [49].

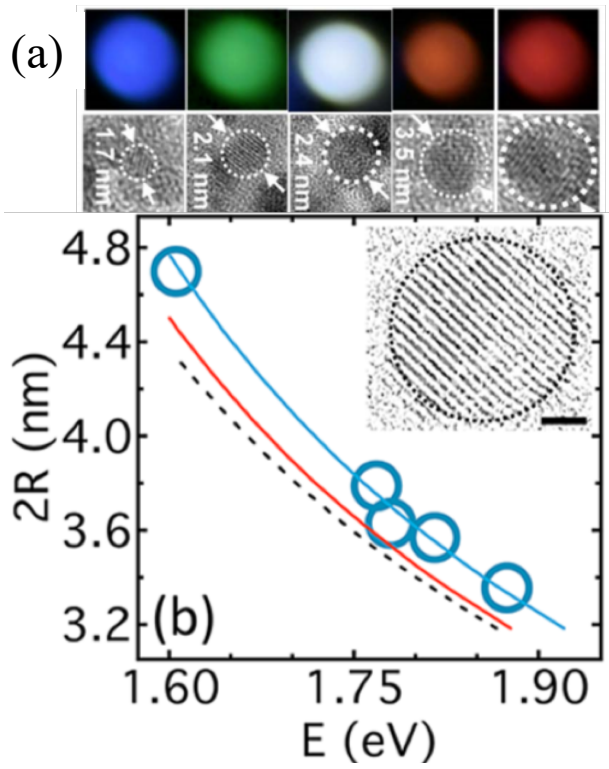

Figure 2.11. Silicon quantum dots emit different colors depending on their size (a) [49]. Band gap energy as function of SiNC diameter for colloidal nanocrystals (b). Reprinted with permission from Ref. [50]. Copyright 2019 American Chemical Society.

3. EXPERIMENTAL PROCEDURE

This Chapter will mainly focus on sample preparation and characterization. The first section (2.2) will cover the preparation of the materials and nanocomposites. The second section (2.3) will be about the characterization methods that we have utilized to analyze the nanocomposites films.

3.1. Nanocomposite Preparation

3.1.1. Polystyrene-SWCNT Triple Bilayer Films

The substrate is an important component of any electronic device, and for a device to be mechanically flexible, the substrate needs to be soft and elastic. The substrates discussed in this dissertation were made out of polydimethyl siloxane (PDMS, Sylgard 184, Sigma-Aldrich). A 10:1 ratio of an elastomer to a crosslinker was prepared. To get a 2 mm final thickness of the PDMS substrate, 13.86 g of the elastomer was thoroughly mixed with 1.38 g of crosslinker. The mixture was then poured into a mold (100 mm x 100 mm) and the mold was placed under 80 kPa vacuum for an hour to remove the air bubbles. The vacuum was then decreased to 40 kPa and the mixture was baked at 90 ℃ for 2 hours. After that, the mold was removed from the vacuum oven and the PDMS was allowed to cool down to room temperature. A PDMS slab with dimensions of 80 mm x 20 mm x 2 mm was cut and cleaned with deionized water and ethanol. Finally, the two ends of the PDMS were clamped in a strain stage, where a pre-strain was applied to the substrate before depositing the nanocomposite films. The strain stage and the PDMS slab are shown in Figure 3.1.

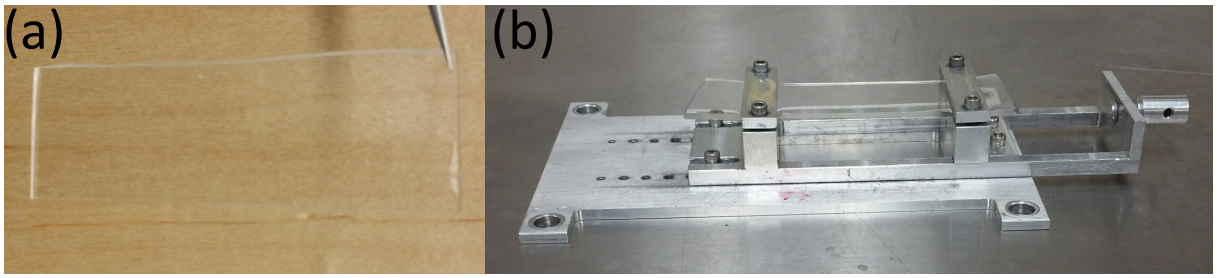

Figure 3.1. A slab of PDMS (a) and the strain stage (b).

Using tip sonication, 1 mg of SWCNT per mL was dispersed in an aqueous solution of 2% mass sodium deoxycholate (DOC) solution. Then, large bundles and impurities were removed by centrifugation for 2 hours at a speed of 21000 rpm [25]. SWCNT thin films with different thicknesses were prepared through vacuum filtration.

Appropriately diluted colloidal SWCNT suspensions were deposited on filter paper to achieve targeted thicknesses of h = 10, 20 and 40 nm. For example, 18 μl of colloidal SWCNT was mixed with 482 μl DI water and 100 μl of this solution was deposited on filter paper starting from the middle of the filter, where the final thickness of SWCNT film on filter paper was around 10 nm. To remove surfactant from the SWCNTs, a 10 % solution of ethanol in water was pulled through the film and filter paper by applying 50 kPa of vacuum pressure until the solvent was gone. Then, we waited at least 30 minutes to make sure that the SWCNT film and filter paper had dried. After that, the SWCNT films on filter paper were cut into small strips with approximate dimensions of 4 mm x 12 mm. A similar procedure was used to get 20 nm and 40 nm films by adjusting the amount of colloidal SWCNT deposited on filter paper. For 20 nm SWCNT films, we mixed 7.2 μl with 492.8 μl while 14.4 μl of colloidal SWCNT was mixed with 485.6 μl to get a 40 nm SWCNT film on filter paper. To get freestanding thin films, three acetone baths were used to dissolve the filter paper followed by three ethanol baths to remove as much (DOC) surfactant from the film as possible. Residual (DOC) surfactant has been shown to

have a detrimental impact on the film's response to an applied strain [6,11]. Figure 3.2 shows a SWCNT film on filter paper, a freestanding film in an ethanol bath, and thin film being transferred by pipette.

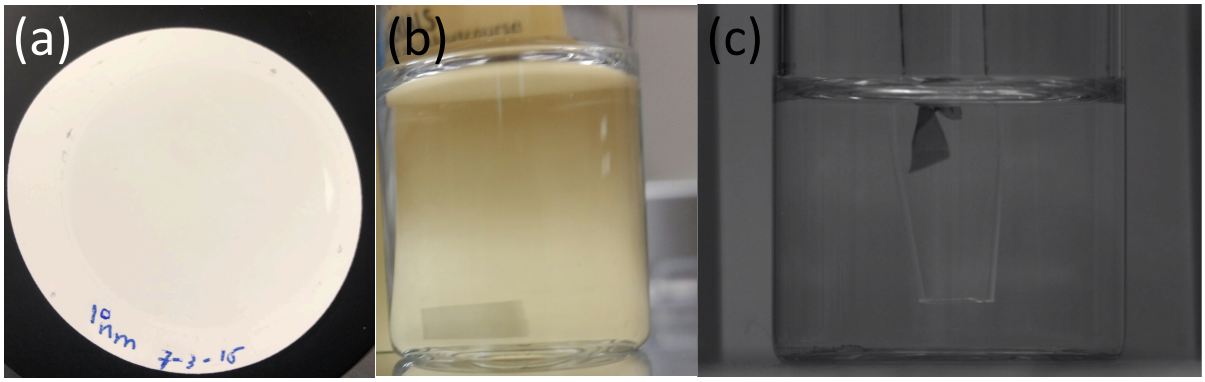

Figure 3.2. SWCNT film on filter paper (a). Freestanding SWCNT film in an ethanol bath (b). Thin SWCNT film transferred by pipette (c) [25].

We used polystyrene thin films (PS) made by spin coating. The Polystyrene used in this experiment was manufactured by Sigma-Aldrich and had a molecular weight of M_w=213 kg/mol. Different PS-in-toluene concentrations were used to get 10, 20 and 40 nm PS films. Three drops of 0.36 %, 0.72 %, and 1.44 % wt. PS in toluene were spin coated onto a clean cleaved mica surface at 3000 rpm for 30 seconds to get 10, 20 and 40 nm PS films, respectively. Then, we cut the PS film in-place on the mica into small squares of 4 mm x 4 mm. The films were then floated off the mica onto the surface of a DI water bath.

Lamellar nanosheets were assembled by first transferring the SWCNT thin film (n = 1) from an ethanol bath using a pipette. The second layer (n = 2), which was a polystyrene thin film, was placed on the SWCNT film by grabbing the PS film gently from a water bath using a piece of mica. All films within a composite were chosen to have comparable thickness. The process was then repeated where the even layers (n = 2, 4, and 6) were PS while the odd layers (n = 1, 3, and 5) were SWCNT. A small portion of each layer was isolated for independent

thickness and wrinkling analysis. Thermal annealing above the glass transition temperature of PS (T = 110 ℃) was applied for 2 hours to ensure PS infiltrated into the porous structure of the SWCNT film. The annealing was done under 50 kPa vacuum. Finally, we took the nanocomposite out of the vacuum oven to cool it down to room temperature, and then compressive strain was applied incrementally (from 1% to 10%) by releasing the prestretch in the PDMS. Three targeted thicknesses (h_0= 10, 20 and 40 nm) with n = 1-6 layers were used in this experiment.

3.1.2. PEDOT:PSS-SWCNT Multilayer Films

In this experiment, a PEDOT:PSS film was assembled between two SWCNT films as a sandwich. The substrate and SWCNT thin films were assembled in the same manner as the first project mentioned in section 3.1.1 while the PEDOT:PSS films were assembled through vacuum filtration. Appreciable amounts of colloidal PEDOT:PSS mixed with DI water were used. The mixture was then deposited on the filter paper, using vacuum filtration (40 kPa) to pull the colloid through the filter once the colored PEDOT:PSS solution was evenly distributed over the filter paper. After deposition, the PEDOT:PSS film on filter paper was dried for 30 minutes. The PEDOT:PSS was then cut into small strips with dimensions of 8 mm x 12 mm and the filter paper was dissolved through three acetone baths. Both SWCNT and PEDOT:PSS films were transferred to and assembled on 15% pre-stretched PDMS substrates using a plastic pipette tip. We started with layer n = 1 (SWCNT) then n = 2 (PEDOT:PSS) and finally n = 3 (SWCNT). All films had comparable thicknesses and three targeted thicknesses (h_0 = 10, 20 and 40 nm) were investigated in separate experiments. We isolated a small portion of each layer for thickness and wrinkling measurements. The layered nanocomposites on the strain stage were baked under

vacuum for an hour at 100 ℃ to ensure all solvent was evaporated. Finally, the nanocomposites were removed from vacuum and cooled to room temperature prior to the application of strain.

In addition, we used three strain cycles to investigate the durability of the PEDOT:PSS-SWCNT- PEDOT:PSS trilayer films. The first cycle was a compressive strain from 2% to 12%, while the second cycle consisted of stretching the multilayers from 4% back to 12 %. The third and final cycle involved relaxing the multilayer films from 2% to 8%. Figure 3.3 shows a schematic of a PEDOT:PSS-SWCNT multilayer film on 15% pre-strained PDMS.

Figure 3.3. Schematic of a PEDOT:PSS-SWCNT multilayer film on 15% pre-strain PDMS.

3.1.3. SWCNT/CdSe NCs Bilayer

SWCNT films were assembled on the pre-stretched PDMS as described in section. 3.1.1, where a pipette was used to transfer the SWCNT film onto pre-strained PDMS. In this project, we investigated the effectiveness of NCs as mechanical stabilizer on a variety of SWCNT films by depositing a monolayer of CdSe nanocrystals (CdSe NCs) in a zero-strain (SWCNT perspective) prestretched configuration. 5 mg/mL of colloidal CdSe NCs dispersed in toluene using hexadecylamine ligands as a surface stabilizer (Sigma-Aldrich Lumidot©). Density-gradient ultracentrifugation (DGU) was then used to purify the NCs by size and remove the excess ligands [26].

A Langmuir-Blodgett (LB) method was used to deposit the CdSe NCs on a SWCNT film adhered to pre-stretched PDMS. It was not possible to cast mixed particle films from a common solvent in a single step, since the SWCNT is suspended in water while the NCs were suspended in organic solvents. First, the SWCNT films were deposited on the pre-stretched PDMS substrate

as described in section 3.1.1, and then 10 μL of DI water was deposited on top of the SWCNT film forming a small droplet. Next, 8 μL of a size-purified chloroform/CdSe NC solution was placed on top of the water droplet. Because the solvents both evaporate at vastly different rates, a NC monolayer is formed on top of the SWCNT film as shown in Figure 3.4 [26]. The final step was applying compressive strain to the bilayer by incrementally releasing the prestrain in the PDMS base, where optical reflection microscope images were collected at each strain for all layers.

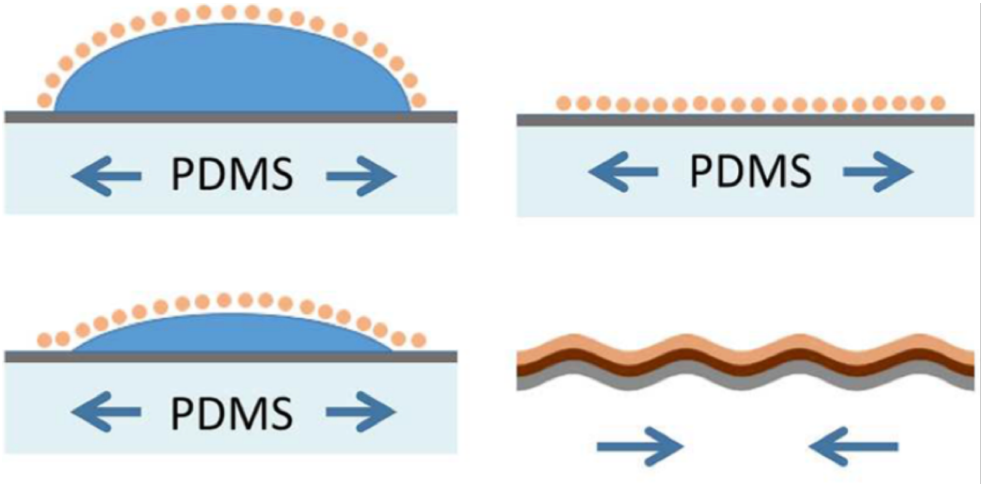

Figure 3.4. Schematic diagram of a SWCNT film coated with CdSe NCs through the Langmuir-Blodgett (LB) method. Reprinted with permission from Ref. [26]. Copyright 2019 American Chemical Society.

3.1.4. SWCNT/Si NC Bilayer

In the fourth project, silicon nanocrystals were used instead of CdSe NCs due to the promising applications of SiNCs in the semiconductor field, as well as their lower toxicity. We investigated the effectiveness of SiNCs for enhancing the elasticity of thin SWCNT films. A non-thermal plasma was used to synthesize SiNCs, which were passivated with 1-dodecene, as detailed in other publications [47,85]. A mixture of chloroform and m-xylene was used to separate the NCs into size-resolved fractions based using the DGU method [86-89].

To assemble the bilayer, a SWCNT film was first transferred onto prestretched PDMS, where we used spray coating to deposit the SiNCs layer. A Kapton mask (polyimide) was used to partially cover the SWCNT film during spraying. The uncovered SWCNT film was adjusted identically down to the spray gun at distance equal to 12 cm. At this distance, we ensured that we had as thin a SiNC layer as possible on top of SWCNT film without dewetting. 20 μL of 4.5% hexane/SiNC solution was airbrushed onto a SWCNT film for three seconds using a commercially available airbrush (Master Airbrush-mini) powered by air under 15 psi pressure. The SWCNT/SiNC bilayer on PDMS mounted in the strain stage was put under vacuum for one hour to ensure all hexane solution was evaporated. We released the strain and took reflection images for pristine SWCNT, SWCNT/NC, and the interface at each applied strain. In this experiment, we investigated five different SWCNT thicknesses of 15 nm, 25 nm, 27 nm, 30 nm and 50 nm.

3.2. Nanocomposite Characterizations

In this section, all characterization methods that were used in this dissertation will be detailed.

3.2.1. Strain-induced Elastic Buckling Instability for Mechanical Measurements (SIEBIMM)

To investigate the mechanical properties of the thin nanocomposite films, we used the SIEBIMM method. Among the other techniques, SIEBIMM has proven to be a cheap and quick method for the mechanical measurement of thin films. Stiff thin films adhered to elastomeric substrates produce periodic wrinkles (buckling pattern) when subjected to a compressive strain, and the wavelength of these periodic wrinkles can be used to deduce the films elasticity [52-54].

The buckling wavelength and the film thickness can be related to the Young's modulus of the compressed film as

$$E_f = (3E_s \frac{(1-v_f^2)}{(1-v_s^2)})(\frac{\lambda}{2\pi h_f})^3 \quad (3.1)$$

where λ is the buckling wavelength, h_f is the film thickness, and v is the Poisson ratio. The plane strain modulus is $\overline{E_i} = \frac{E_i}{1-v_i^2}$ where i is either *s* for the substrate or *f* for the film [25-26,52-54,73,74].

The SIEBIMM method has been widely utilized as a characterization technique to extract the Young's modulus of thin homogenous films such as polymers. In addition, it has been applied to complex structures such as polyelectrolyte multilayers [52].

SIEBIMM is a linear model, and when applied to a homogeneous thin film it predicts harmonic wrinkles. However, SWCNT films produce disordered wrinkles due to quenched fluctuations in SWCNT film thickness [54-56]. Recently, Harris, et al. have done extensive work to apply this method to thin SWCNT films, where it was argued that SIEBIMM can also be used to quantify inhomogenous films such as SWCNT films. The wrinkles in thin SWCNT films can be modeled through random thickness fluctuations [55,56]. This disorder produces higher amplitude wrinkles that are further apart, in comparison to the usual wrinkles that are fainter and have a periodic structure [25]. These fainter wrinkles – which show strong regular periodicity – are our target for extracting the buckling wavelength, and we refer to these wrinkles as having the fundamental wrinkling wavelength λ. We used optical reflection microscopy to image the wrinkled films. Film thickness was measure by two approaches: atomic force microscopy and light transmission/extinction using a broadband lamp for excitation and a spectrometer for light

detection. Figure 3.5 shows the wrinkling behavior of polymer, SWCNT, and polymer-SWCNT bilayer films.

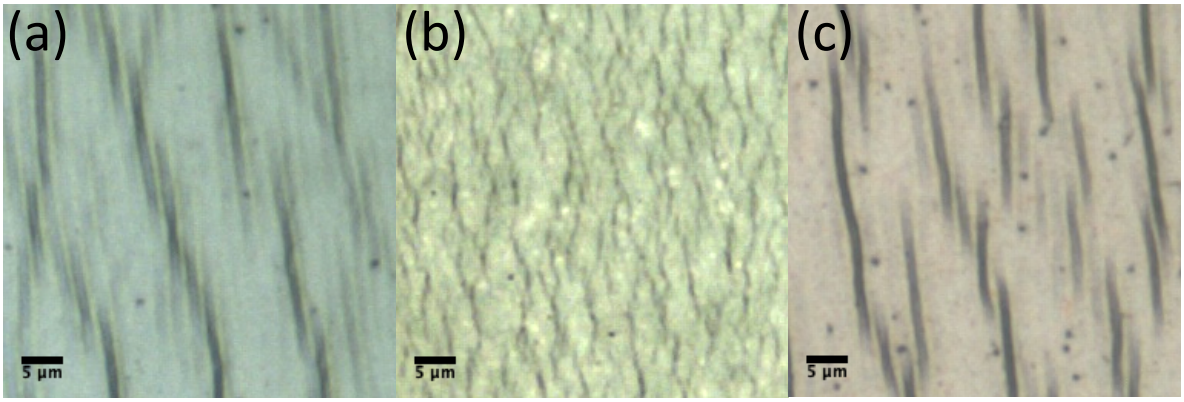

Figure 3.5. A 20 nm PEDOT:PSS film (a). A 20 nm SWCNT film (b). A bilayer of SWCNT-PEDOTS:PSS (10 nm each film) (c). All films are at 2% applied strain in the horizontal direction.

To extract the fundamental wrinkling wavelength λ, a perpendicular line was drawn through the faint wrinkles (ImageJ) and the distance between each fundamental wrinkle was measured in pixels. The wavelength values were then converted to μm, in which at least three lines were drawn at each image to average the wavelength values.

More quantitatively, the two-point height-height correlation function $c(\mathbf{r}) = \langle u(\mathbf{r})u(0)\rangle$ has also been used to extract the wrinkling wavelengths. The projection along the strain direction, $c(x)$ has peaks at $x = \lambda$, 2λ, or 4λ [56]. ImageJ was used to compute the correlation functions from thresholded binary images, averaging together correlation results from four images, each 250 by 250 pixels in size. In some cases, we had to account the doubling and quadrupling of the wavelength because the fundamental wavelength became smaller at higher strain for thinner films [25]. Figure 3.6 shows how λ can evolve to 2λ or 4λ in some cases. Figure 3.7 shows the correlated image and a typical plot of the correlation function, where the bottom panel indicates a scenario where λ goes to 4λ.

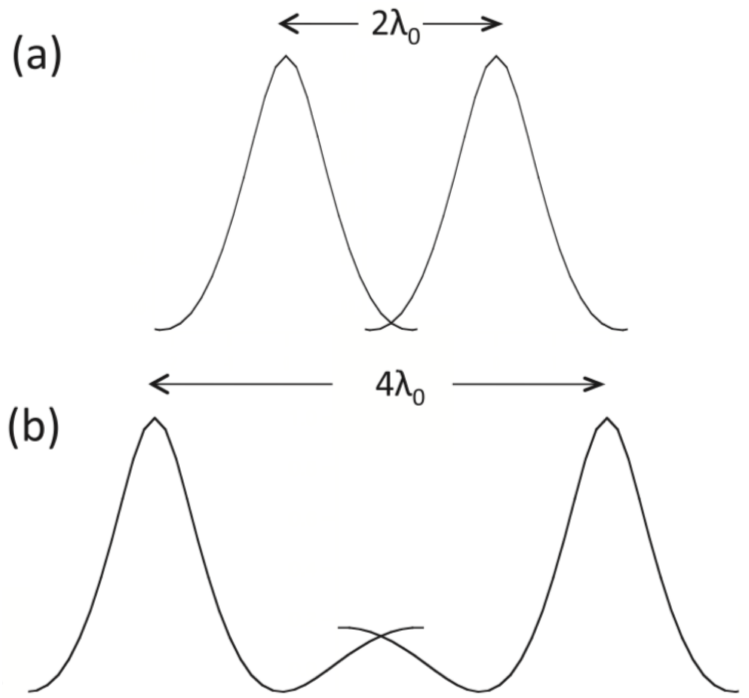

Figure 3.6. Schematic diagram of λ going to 2λ or 4λ [56].

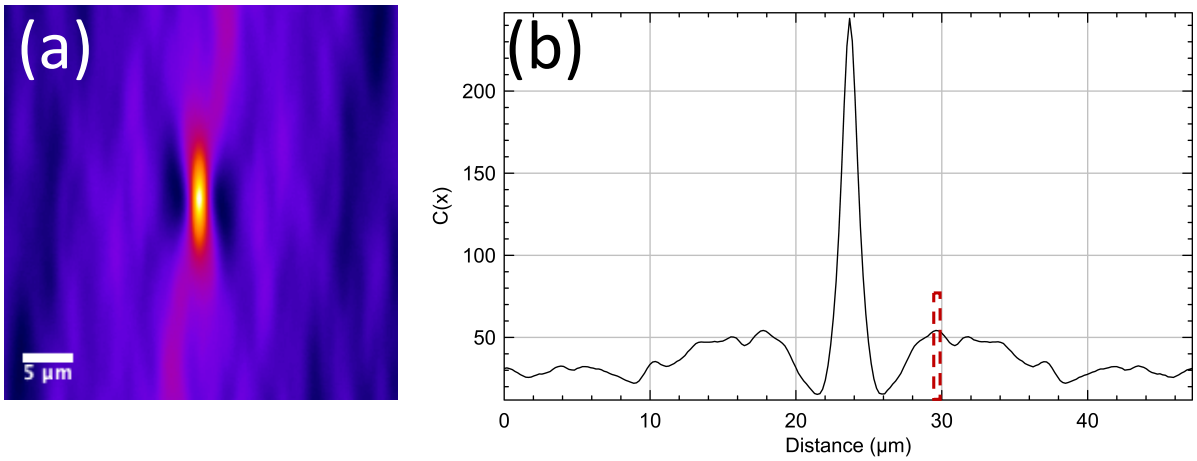

Figure 3.7. 2D correlation-function image (a). The x-projection of $c(x)$ indicating λ going to 4λ (b).

3.2.2. Reflection Optical Microscope

Reflection optical microscopy was used to determine the wrinkling wavelength of SWCNT films and the nanocomposites at all strains. We utilized an Olympus BX51 microscope with 50x lens in bright field mode. For the polymer-SWCNT multilayer projects, we took two

images for each layer at each strain. For the SWCNT/NC bilayers, we captured two images for pristine SWCNT, SWCNT/NC, and the interface between the two surfaces. This was also done at each strain.

3.2.3. Atomic Force Microscope

AFM was used in all projects to determine the SWCNT, PS, NC, and PEDOT:PSS film thicknesses. A Veeco DI-3100 atomic force microscope was utilized in tapping mode. A 10 nm radius tip was used to measure the film thickness. We measured at least three different spots (step heights) for each film, and we slope-corrected the profiles to obtain average step heights. We were able to obtain AFM images for the nanocomposites on a variety of substrates such as wafer Si, glass, and PDMS. In addition, the NC thickness was also measured at the SWCNT-NC interface.

Furthermore, AFM was used to determine the aspect ratio of individual SWCNTs and the wrinkling amplitude of the nanocomposites at 10% applied strain. To measure the aspect ratio, we immersed a small chip from a silicon wafer for 24 h in a refrigerated solution consisting of 30 μL of colloidal SWCNT mixed with 150 μL of DI water. The silicon chip was then soaked in ethanol for 2 h before measurement. To obtain good images for SWCNT length and width measurements, we increased the scan line resolution from 256 to 512 and we decreased the scan size to 10 μm. The wrinkling amplitude was measured using AFM for nanocomposites at 10% applied strain. To do that, we removed the nanocomposites from the strain stage after we released the strain at 10% from a prestretched position.

3.2.4. Optical Transmission of Thin Films

SWCNT film thickness is critical and important when applying SIEBIMM because film thickness enters the modulus to the power of three. We used other approaches to determine film

thickness beyond AFM. Specifically, SWCNT films were deposited on glass cover slips where the step heights were measured by AFM. Simultaneously, the optical extinction of the SWCNT films was determined in transmission using a broadband lamp for excitation and a spectrometer (Ocean Optics QE65000) for light detection at a wavelength of 583 nm. In this approach, we applied the Beer-Lambert law for varied SWCNT film thicknesses, $I(h) = I_0 e^{(-\alpha h)}$, where I is the transmitted intensity and I_0 is the incident intensity at the extinction wavelength. This provided us with the extinction coefficient α. The power of this approach is that after calibration, it allowed us to optically measure the local thickness of SWCNT films *in situ* without AFM. The same approach was applied to PEDOT:PSS films where we optically measured the films thickness after determining the extinction coefficient α for PEDOT:PSS at a wavelength of 650 nm. Figure 3.8 shows the optical extinction curve as function of SWCNT thickness.

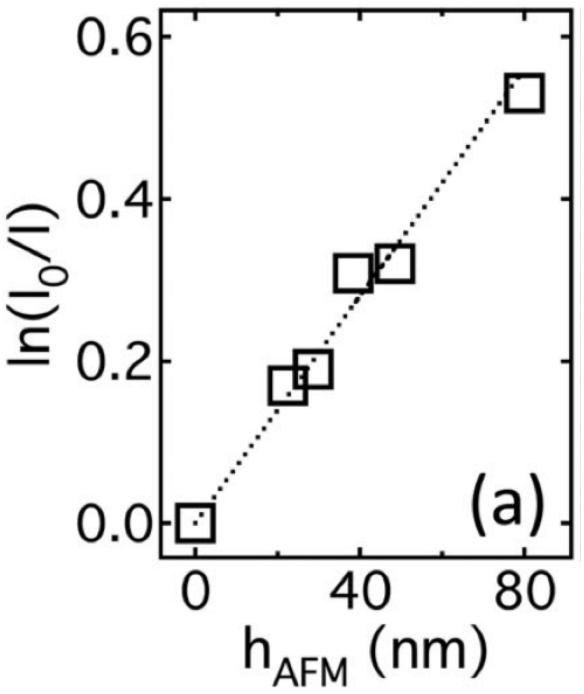

Figure 3.8. The optical extinction curve as function of SWCNT thickness [25].

3.2.5. Photoluminescence Microscopy

We used photoluminescence (PL) microscopy to study the PL emission from NCs and to quantify the thickness of NCs coated on SWCNT films. Quantum dots (QDs) can emit light at certain wavelengths depending on their size and shape and PL intensity can be used to determine NC size [57, 58]. In our experiment, we used PL images and peak spectral emission strength to determine NC layer thickness on SWCNT films [26]. Figure 3.9 shows the PL spectra of the colloidal CdSe NC fraction that was used in SWCNT/CdSe NCs bilayer project [26].

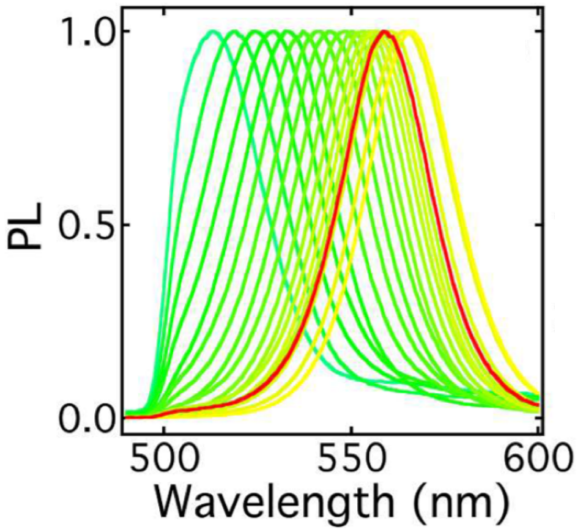

Figure 3.9. The PL spectra of the colloidal CdSe NC fraction. Reprinted with permission from Ref. [26]. Copyright 2019 American Chemical Society.

3.2.6. Transmission Electron Microscopy

TEM was utilized to determine NCs size, to characterize the morphology of the SWCNT films and SWCNT/NC bilayers, and to gain insight into the characteristic width of the SWCNT-polymer interface. We used a JEOL JEM-2100 analytical TEM (200 kV) with a GATAN Orius SC1000 CCD. TEM provided us with useful information about the size and shape of NCs. Figure 3.10 shows a TEM image of a single CdSe NC and NC diameter histogram [26]

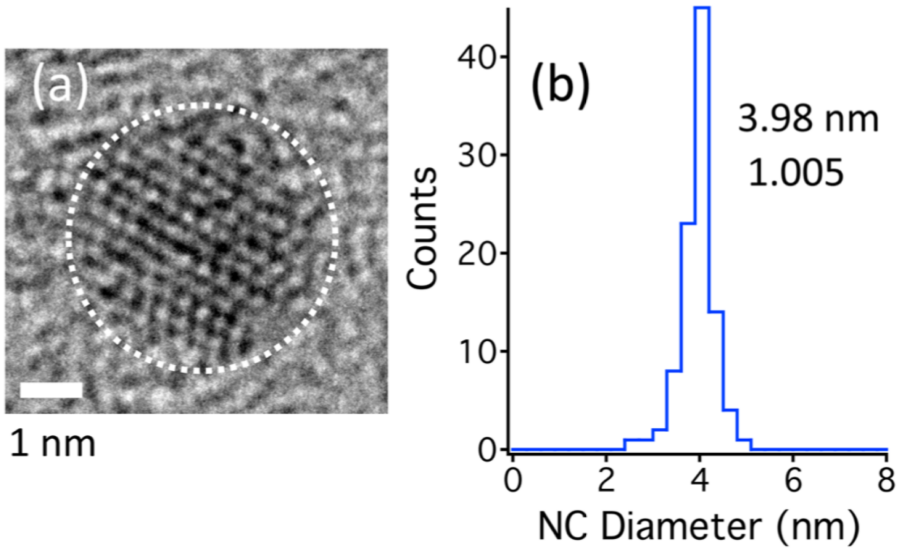

Figure 3.10. A TEM image of a single CdSe NC showing how NC size is extracted from TEM images using ImageJ (a). CdSe NC diameter histogram shows that the mean NC size is 3.98 nm, with a polydispersity index of 1.005. (b). Reprinted with permission from Ref. [26]. Copyright 2019 American Chemical Society.

In addition, we used TEM to investigate the interfacial structure of SWCNT coated with thin polymer films, from which we were able to determine the interfacial thickness [25].

3.2.7. Tensile Tester

The Young's modulus of PDMS substrates was measured using an Instron 5545 Tensile Tester with a load of 100 N. The small-strain slope of the linear part of the stress-strain curve was used to extract the Young's modulus. The Young's modulus for all PDMS substrates that we used was ($1.4 \leq E_s \leq 2.5$ MPa) and the value measured for a specific substrate was used in the wrinkling analysis of a given film.

4. THE RIGIDITY OF SWCNT-POLYMER MULTILAYER NANOCOMPOSITES

4.1. Introduction

Polymer nanocomposite hybrid ‘soft’-‘hard’ materials with enhanced mechanical and transport characteristics are one of the most expansive and diverse themes in the broader field of nanotechnology. In particular, SWCNTs as hard materials are uniquely polymer-like in their own right and can be used for a wide range of applications, including transparent conducting films and field-effect transistors. In polymer nanocomposites, SWCNTs can impart outstanding transport characteristics to a polymer matrix at relatively low volume fractions [25].

An emerging theme in polymer science and nanotechnology is the use of SWCNTs as a phase in a sheet-like morphology, since this provides a rather simple structure that can be readily processed and modeled. Intuitively, a layered structure also offers a large interfacial contact area, without the need to focus on the true state of nanotube dispersion in the matrix, which in most practical scenarios is not ideal. In general, as the sheet thickness starts to approach the nanoscale, we can expect the properties of the composite to be altered in ways that reflect how the SWCNT–polymer interaction is modified at the nanoscale. In the limit of a small number of layers, a lamellar nanosheet also offers a structural paradigm for a large number of hybrid or heterojunction morphologies, with particular relevance to applications in flexible electronics [25].

On a more fundamental level, measuring the mechanical properties of thin films offers an interesting and challenging problem in polymer science and nanotechnology, specifically in the context of a thin stiff film adhered to a thick soft substrate [25]. A strain-induced wrinkling approach has proven to be a powerful method to query the mechanical properties of nanoscale

thin films, and this method can also be used to query the elastic response of high-order structures, such as multilayered nanocomposite films [25].

In our experiment, we used the wrinkling approach to study the mechanical properties of flexible SWCNT-polymer lamellar nanosheets. Using the deposition techniques detailed previously, alternating layers of SWCNT and polymer were transferred through fluid assembly. Both the elastoplastic behavior of flexible SWCNT films and the impact of film structure (e.g. thickness and composition) were investigated using the wrinkling approach. In our notation, n = 1 corresponds to a pure SWCNT film, n = 2 denotes a SWCNT/polymer bilayer, n = 3 corresponds to SWCNT-polymer-SWCNT, and n = 4 denotes SWCNT-polymer-SWCNT-polymer, etc., with all layers in a sheet having a common targeted thickness h_0. The results that showed the greatest mechanical synergy between SWCNT and polymer nanosheet were for nanosheet thicknesses $h_0 \leq 20\ nm$. We explained this enhanced mechanical synergy by focusing on the magnitude of the layer thickness, h_0, in comparison to the characteristic interfacial width, w. For all values of layer thickness, a comparison with a simple rule of mixtures suggested that the nanosheets have reached the bulk limit by n = 6. These results have potential significance for controlling the durability and rigidity of thin hybrid SWCNT films [25].

4.2. Materials and Methods

The experimental procedures are described in section 3.1.1.

4.3. Results and Discussion

The lamellar nanosheets were assembled by first pipetting a pure SWCNT film from an ethanol bath onto the clean surface of a pre-stretched PDMS substrate. The next layer (n = 2) was deposited by collecting a polymer film of comparable thickness from the surface of a DI water bath using a piece of mica and gently depositing it on the SWCNT film. The process was then

repeated, where the odd layer was SWCNT (n = 1, 3, 5) and the even layer was polymer (n = 2, 4, 6). In addition to making the composite, we also isolated a small portion of each film to facilitate thickness and wrinkling wavelength measurements, as described in section 3.1.1 [25].

We considered three targeted layer thicknesses: h_0 = 10, 20 and 40 nm, with n = 6 in total for each experiment. After thermal annealing, the strain in the PDMS was released incrementally, and multiple reflection optical micrographs were taken at each strain for each layer. The nanocomposite was treated as a homogenous film with no slip or delamination. Specifically, we have used the fundamental wrinkling wavelength λ to calculate the modulus using equation 3.1 [25].

Figure 4.1 shows the strain dependent modulus for each value of n at each targeted value of h_0, where the legend in Figure 4.1 applies to each panel. For many of the films, we observe signatures of the strain softening typical of compressed SWCNT films. Specifically, for the pure SWCNT (n = 1) at all thicknesses, and for the bilayer (n = 2) at the smallest h_0. This behavior has been explored, and it was suggested that it arises from rearrangements in the SWCNT network in response to the applied strain [25]. For all three values of the target thickness h_0, the response resembles purely elastic behavior as the number of layers increases [25]. In addition, we observe that the Young's modulus of PS thin films increases with respect to film thickness as shown in Figure 4.1, dashed line.

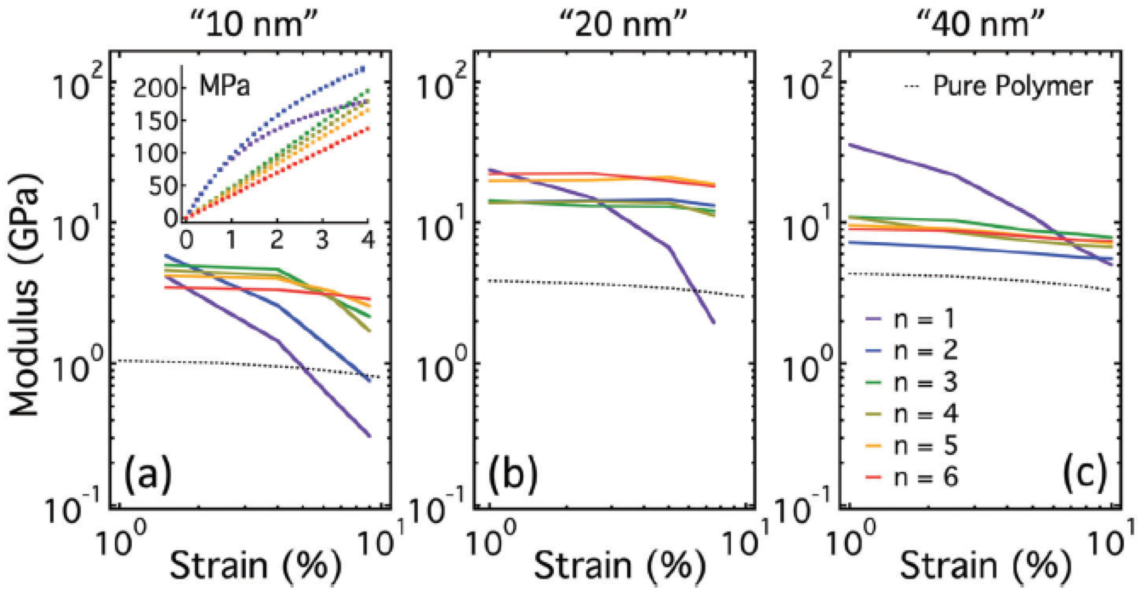

Figure 4.1. Strain dependent modulus of 10 nm nanocomposites (a), 20 nm nanocomposites (b), and 40 nm nanocomposites (c) [25].

In Figure 4.2, the modulus for n = 6 is intermediate to the moduli of the pure materials. To quantify this, the lamellar geometry is ideal for applying a simple rule of mixtures [25,100]. Uniform strain (ideal behavior) is used to model the upper bound, $E_{\parallel} = \phi E_{CNT} + (1-\phi)E_{Poly}$, while the uniform stress (non-ideal behavior) is used to model the lower bound, $1/E_{\perp} = \phi/E_{CNT} + (1-\phi)/E_{Poly}$. Because the layers of a nanosheet all have close to a common thickness, h_0, we use 0.5 for the volume fraction (ϕ). We also use the measured SWCNT (purple curve, Figure 4.2) and polymer (gray curve, Figure 4.2) modulus for E_{CNT} and E_{Poly}, respectively. The resulting upper and lower bounds are shown in Figure 4.2 (black dashed line) [25].

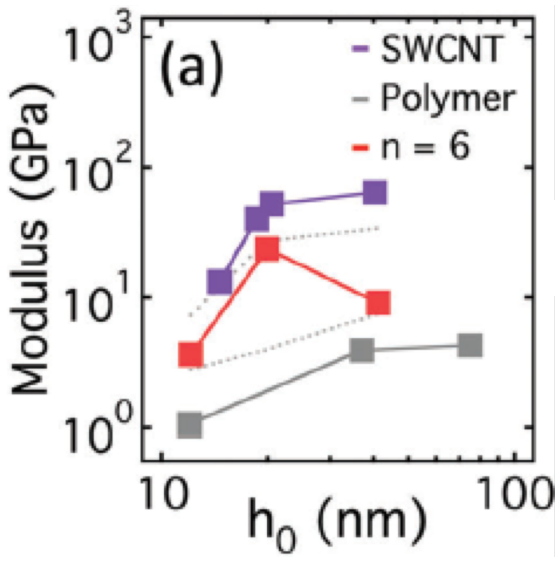

Figure 4.2. Extrapolated zero-strain modulus as a function of layer thickness for the SWCNT (n = 1), pure PS, and the triple bilayer composite (n = 6). The dashed lines are the upper and lower bounds [25]

Our results suggest that lamellar nanosheets have reached the bulk limit by n = 6 for thicknesses of 10 nm ≤ h_0 ≤ 40 nm, based on a comparison with a simple rule of mixtures in Figure 4.2 [25]. The results also suggested that 20 nm lamellar nanosheets show a unique response. This can be seen in Figure 4.2 where the modulus of n = 6 for the 20 nm experiment exhibits nearly ideal behavior [25].

A somewhat similar effect was observed by Semler et al, who focused on the interfacial width of a SWCNT-polymer bilayer [28]. In that work, they associated the better mechanical performance with layer thicknesses near the characteristic interfacial width w, where TEM was used to extract the thickness of the interpenetration layer h_{IP}. For comparison, the interfacial width was estimated through $w = \frac{a}{\sqrt{\chi}}$ in terms of an effective Flory-Huggins interaction parameter χ and a characteristic length scale of the mixture a. The interactions include SWCNT-polymer, SWCNT-SWCNT, and polymer-polymer. The estimate of characteristic width based on this model was $w \approx 20 - 30\ nm$, which we suggest explains why the 20 nm experiment showed

better performance. Figure 4.3 shows TEM images of the SWCNT-polymer interface, where the interpenetration depth is indicated [25, 28].

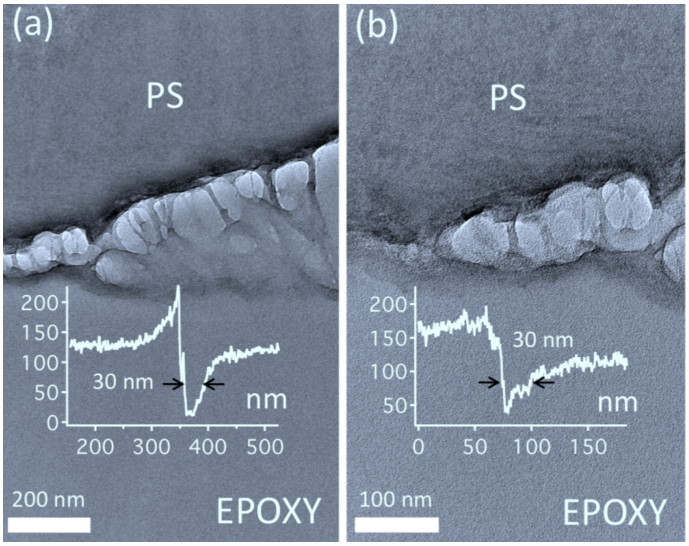

Figure 4.3. TEM image of a SWCNT-polymer interface with a characteristic thickness of 30 nm [28].

In our findings, the interaction between SWCNT and polymer could be seen in two ways. First, the modulus of nanocomposite thin films could be enhanced in an ideal manner. Second, the reduction in SWCNT film modulus (i.e., strain softening) was reduced using soft, elastic fillers such as a polymer. We attribute this enhancement to the effects of excluded-volume in a semi-porous structure in a SWCNT network. The polymer filler reduces the ability of SWCNT bundles to rearrange [25].

4.4. Conclusion

In conclusion, the wrinkling approach was used to examine the mechanical properties of lamellar nanosheets, where the Young's modulus was specifically extracted from the data. In addition, the elastoplastic behavior of the lamellar nanosheets was investigated as function of the number of layers and film thickness. At h_0 = 20 nm and below, the nanosheets showed ideal behavior with reduced strain softening. The optimal diffusion width between polymer and

SWCNT at the interface occurs at 20 nm lamellae thickness, which was explained through the characteristic interfacial width w between the two immiscible phases. The nanocomposites fabricated at thicknesses of 10 nm $\leq h_0 \leq$ 40 nm have realized their bulk limit by n = 6 based on a comparison with a simple rule of mixtures. The results demonstrate an easy way to control the rigidity and the durability of a layered hybrid structure for many applications, including flexible electronic devices [25].

5. DURABLE CONDUCTING TRANSPARENT SWCNT-PEDOT:PSS MULTILAYER FILMS FOR FLEXIBLE ELECTRODES

5.1. Introduction

Transparent conductive electrodes (TCEs) play a critical role in optoelectronics such as light emitting diodes (LEDs), touch screens and solar cells. TCEs work as windows for optoelectronic devices, which also allow light to go through the device. In addition, they either extract holes or electrons from the active area. Right now, indium tin oxide (ITO) is commonly used as a TCE. However, ITO is facing two main challenges. First, ITO is costly because indium is becoming a rare material. Second, ITO glass is fragile while modern electronics is moving toward flexible skin-like devices, and ITO is not suitable for such applications due to its rigidity and brittleness. A substitute for ITO should maintain its conductivity under deformation. In addition, any new material is required to meet minimum electronic standards, which are low sheet resistance (less than 100 $\Omega/_{sq}$) as well as high optical transparency in the visible region of the electromagnetic spectrum [60].

Single walled carbon nanotubes (SWCNT) and their composites have received much attention because of their outstanding properties. High Young's modulus ($\sim$ 1.2 TPa) and strength, high conductivity, and optical transparency for sufficiently thin films are the attractive properties that make SWCNTs suitable for TCEs [25,60]. In simple terms, SWCNTs are graphene sheets rolled up into a tube, which can be either metallic or semiconductor depending on the molecular symmetry of the SWCNT [25]. These quoted properties are for individual SWCNTs, while SWCNT networks show reduced properties. However, using a sheet-like morphology for SWCNTs would provide a large contact area and precise thickness control [25].

Undoped SWCNT films have shown conductivities of 1.5×10^4 S/m, where the minimum standard for ITO replacement requires values higher than 5.3×10^5 S/m coupled with high optical transparency (above 90%) [59, 60]. However, the conductivity of SWCNT films can be improved by acid treatment and gold chloride doping, for example, but these treatments may negatively affect the active layer in such organic LED applications [27, 60].

Extensive work has been done to incorporate SWCNTs into conductive polymers such as poly(3,4-ethylenedioxythiophene)-poly(styrenesulfonate) (PEDOT:PSS), and PEDOT:PSS can impart high conductivity and flexibility to SWCNT networks by bridging adjacent CNTs. The conductivity of PEDOT:PSS thick films have reached up to 4100 S/cm under strain [31], and the films show durability when subjected to 1000 strain cycles up to 100% applied strain, while the film conductivity was constant at ~ 3600 S/cm [31]. However, PEDOT:PSS is environmentally sensitive and can be degraded by UV-light while its conductivity can be affected negatively by moisture [12]. Protecting PEDOT:PSS films from the environment is necessary in order to make them applicable to electronics, and this can be done through the thermal treatment of PEDOT:PSS thin films [12, 38].

Recently, an increasing number of studies have provided excellent results for SWCNT-PEDOT:PSS composite films. De, et al. showed film conductivities of up to 10^5 S/m with optical transparency above 80% at 0.55% volume fraction of SWCNT mixed with PEDOT:PSS [60]. However, the precise control of the dispersion state, which in most practical scenarios is far from ideal, renders the composites challenging to make. Intuitively, a layered structure of SWCNT as a thin film offers a large interfacial contact area, but without the need to focus on the true state of nanotube dispersion [25].

Based on the results of the previous Chapter, a SWCNT-PEDOT:PSS multilayer approach might control both the conductivity and the rigidity of the composites. Previously, SWCNT thin films coated with polystyrene thin films have shown a significant enhancement in their ability to resist strain softening. We attributed this to the filling the porous structure of SWCNT film by a second nanomaterial (PS). PS infiltrated into the porous structure of the SWCNT film to prevent the SWCNTs from bundling and realignment in response to an applied strain [25].

In this work, we have sandwiched an active polymer filler (i.e., a PEDOT:PSS thin film) between two SWCNT films on a pre-stretched elastic substrate. We measured the Young's modulus as function of the applied strain for each layer by utilizing the wrinkling approach. Specifically, we studied the mechanics of each layer as function of the film thickness. Three strain cycles were applied to study the durability of the nanocomposites, where the first cycle was a compressive strain, the second cycle was stretching, and the third cycle was compressing the composites back to the initial state. Three nanocomposites have been investigated in this work, where each one had different thickness while all layers in each composite had a common thickness h_0. For a 10 nm composite, n = 1 corresponds to a SWCNT film with a thickness of 10 nm, while n = 2 was a 10 nm thick PEDOT:PSS film. The last layer for the 10 nm experiment was a 10 nm thick SWCNT film, which we denote as n = 3, and so on for 20 and 40 nm composites. We found that the greatest mechanical synergy between SWCNT and PEDOT:PSS occurred for $h_0 \leq 20\,nm$ at all strain cycles, which we again attribute to a characteristic interfacial width, w, and to the interpenetration of PEDOT:PSS into the porous structure of a SWCNT network. In addition, the thin PEDOT:PSS film acted as a plasticizer for thicker SWCNT film (40 nm), where it decreased the SWCNT film modulus and increased the SWCNT

film yield strain. Our results have potentially useful implications for controlling the rigidity and durability of thin hybrid films and heterojunctions based on multilayer conductive films.

5.2. Materials and Methods

The experimental procedure was described in section 3.1.2.

5.3. Results and Discussion

The multilayer films were assembled by pipetting SWCNT and PEDOT:PSS films from an ethanol bath to a pre-stretched PDMS substrate. The bilayer (n = 2) was then coated with a second SWCNT film (n = 3), where we isolated a small portion for each layer to facilitate wrinkling and thickness measurements. In our experiment, all films had a common thickness h_0. Figure 5.1a-c shows a schematic diagram for all three cycles, where we captured two images for all strains at each layer.

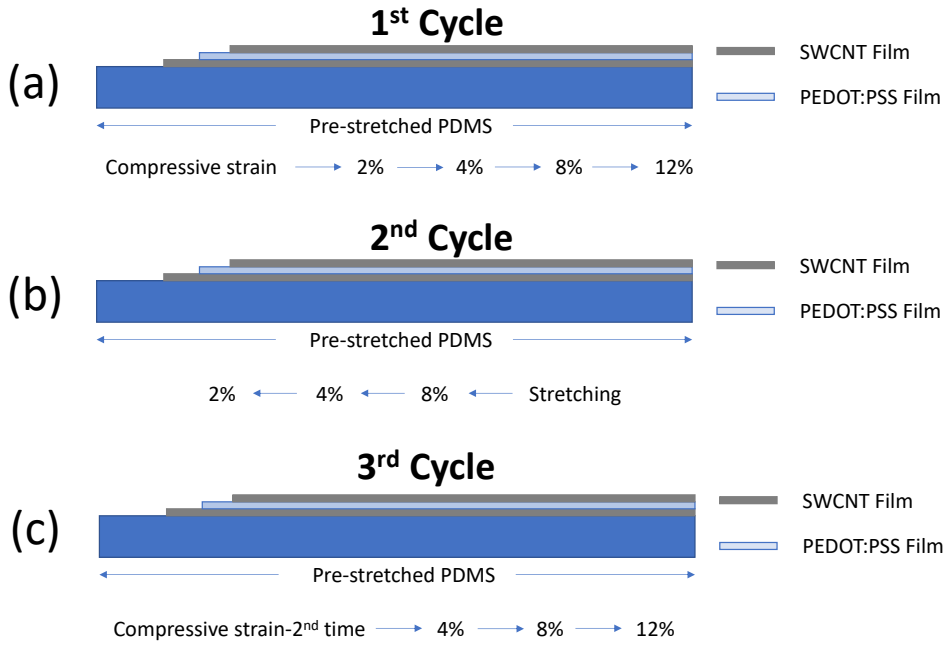

Figure 5.1. Schematic diagram of three strain cycles of the SWCNT-PEDOT:PSS multilayers: 1st strain cycle (a), 2nd strain cycle (b), 3rd strain cycle (c).

The second important factor here is the film thickness. We have used two approaches: AFM and optical transmission, as noted in 3.2.3 and 3.2.4, respectively. Figure 5.2a shows an AFM image of the edge of a PEDOT:PSS film, while Figure 5.2b shows the step height of the PEDOT:PSS film (32 nm). In addition, we used optical transmission to find the extinction as a function of film thickness for a variety of PEDOT:PSS film thicknesses to get the extinction coefficient α, as shown in Figure 5.2c.

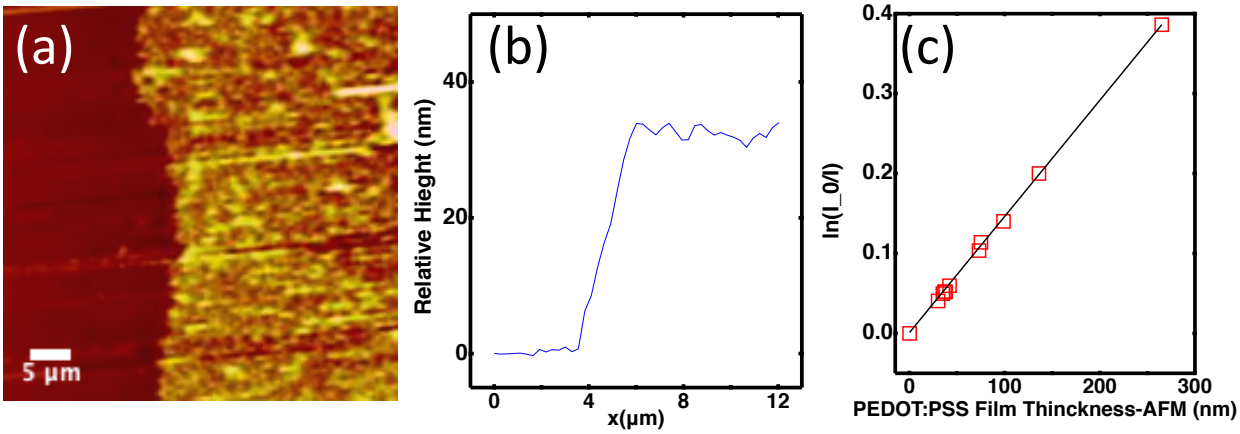

Figure 5.2. AFM image of a PEDOT:PSS thin film (a). Step height of a 32 nm PEDOT:PSS film (b). Optical extinction curve as a function of PEDOT:PSS film thickness from AFM (c).

To find the Young's modulus, we utilized SIEBIMM as noted in section 3.2.1 and equation 3.1, which assumes good adhesion between all the layers. Figure 5.3 shows optical reflection images of the 20 nm experiment, showing all strain cycles for each layer.

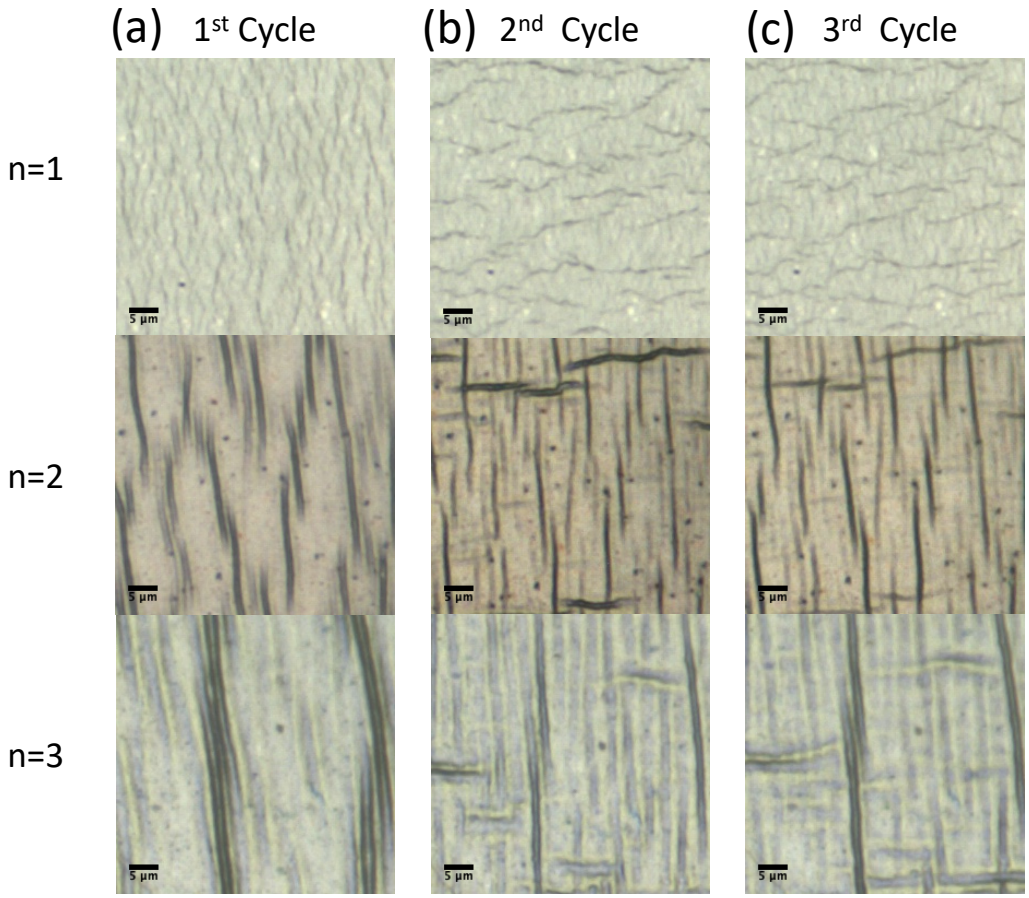

Figure 5.3. Optical reflection images of 20 nm SWCNT-PEDOT:PSS multilayers: 1st cycle (a), 2nd cycle (b), and 3rd cycle (c) at 4% applied strain in the horizontal direction.

The strain dependent modulus for each layer at each targeted thickness h_0 is shown in Figure 5.4a-c. Interestingly, we observed that the modulus of PEDOT:PSS films dropped slightly with a decrease in the films thickness [25], which we attribute to a reduction in the crystalline structure of PEDO:PSS [64,71]. In general, PEDOT:PSS has a semi-crystalline structure, where PEDOT forms a semi-crystalline polymer and PSS is an amorphous polymer [61-65,71]. In PEDOT:PSS films, the number of PEDOT chains is lower than PSS chains. Thus, reducing the film thickness leads to a decrease in the amount of PEDOT in the system, which reduces the percentage of crystalline structure [34,61-65].

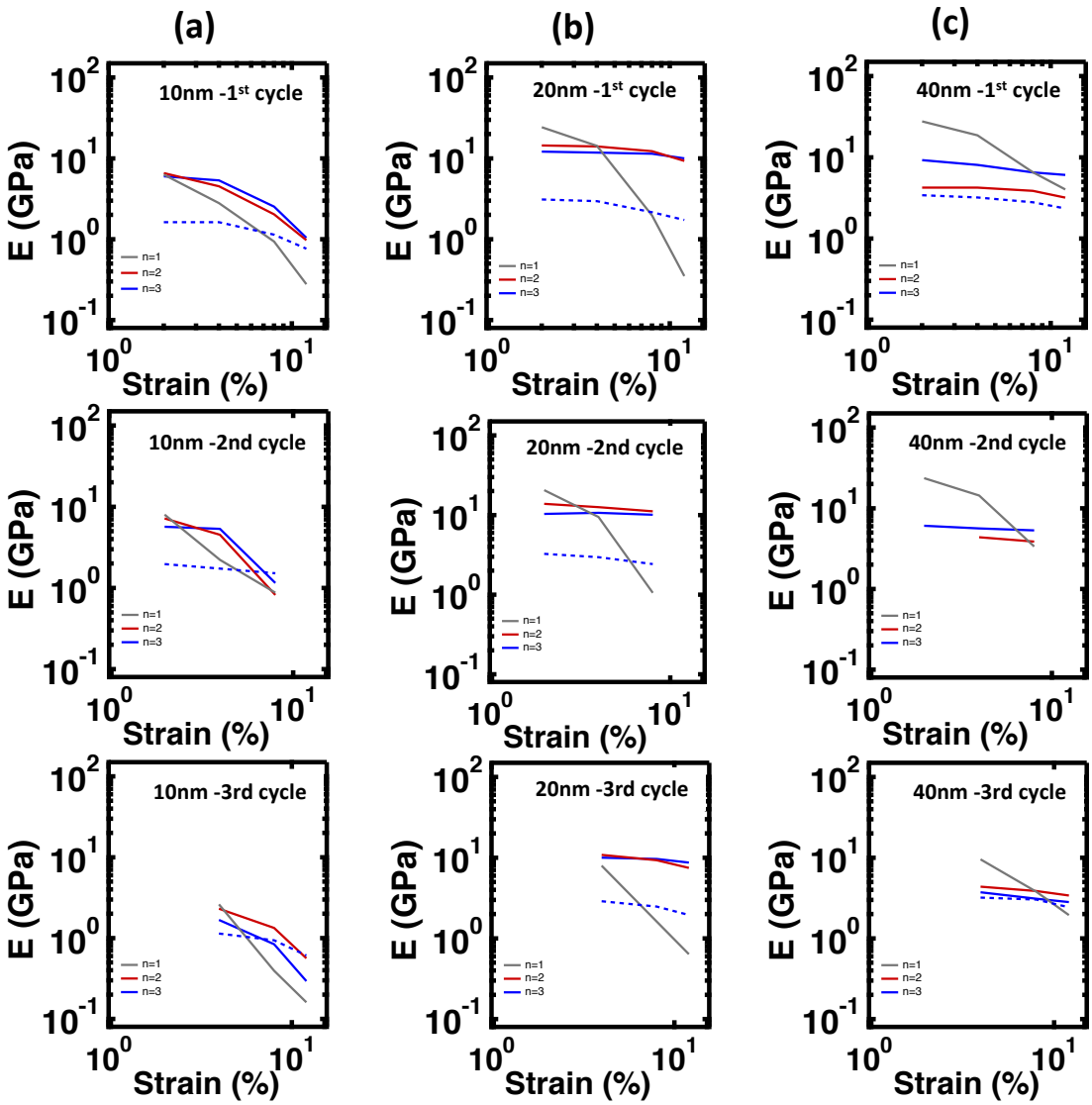

Figure 5.4. Strain dependent modulus for each layer at each targeted thickness h_0: 10 nm (a), 20 nm (b), and 40 nm (c). 1st row is 1st strain cycle, 2nd row is 2nd cycle, and 3rd row is 3rd strain cycle.

In addition, it was obvious that $n = 1$ for all experiments shows strong strain softening. However, the strain softening was reduced for SWCNT-PEDOT:PSS nanocomposites once the number of layers increased. Previously, we attributed this to the excluded volume effect where filling the porous structure of the SWCNT film reduced the strain softening by preventing the rearrangement of SWCNTs in response to the applied strain [25]. Compared to all other

experiments, the 20 nm experiment shows the most durable composite films, where the strain softening was reduced for all cycles as the number of the layers increased. In addition, the PEDOT:PSS film enhanced the elasticity of the 20 nm SWCNT film where the Young's modulus increased for the second and third layer. Again, we attribute the enhancement to the layer thickness approaching the characteristic interfacial width between the two materials. PEDOT:PSS fills the porous structure of the SWCNT network rather than forming sharp interface. Figure 5.5 shows an example of this for a TEM image of the interfacial adhesion between polymer and SWCNT films [25,28]. We attribute the PDOT:PSS results to a similar effect.

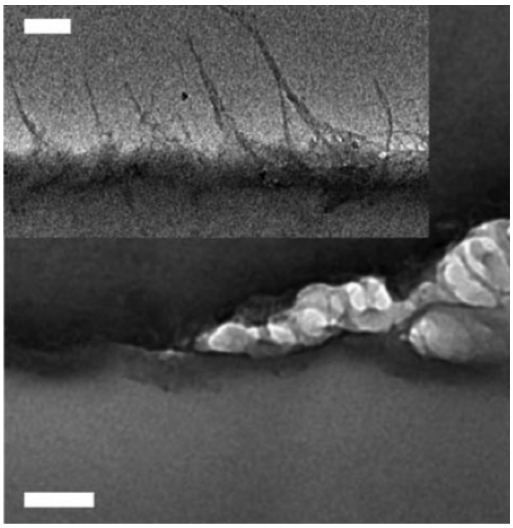

Figure 5.5. TEM image of SWCNT-Polymer interface [25].

However, the 10 nm experiment showed a reduction in the Young's modulus even with an increase in the number of layers. This was explained by the thickness fluctuations in the ultrathin SWCNT films when the films started to approach the percolation threshold: significant fluctuations in thickness couple strongly to the rigidity of the layers and decrease performance. The 2D percolation threshold of the SWCNT films used in this study is around 10 nm, and there is limited enhancement in mechanical properties for a film that is thinner than 10 nm [25].

In addition, 40 nm showed a reduction in strain softening but the Young's modulus was reduced. In this case, the polymer film acted as plasticizer. PEDOT:PSS reduced the modulus but enhanced the yield strain [25,28]. It is obvious in Figure 5.6 that PEDOT:PSS thin film has eliminated the wrinkles in the second layer of the 40 nm experiment at the second strain cycle. Here, the PEDOT:PSS film also reduced adhesion between the bilayer and the substrate due to less favorable interactions between PEDOT:PSS and SWCNT at 40 nm thick films [25,28].

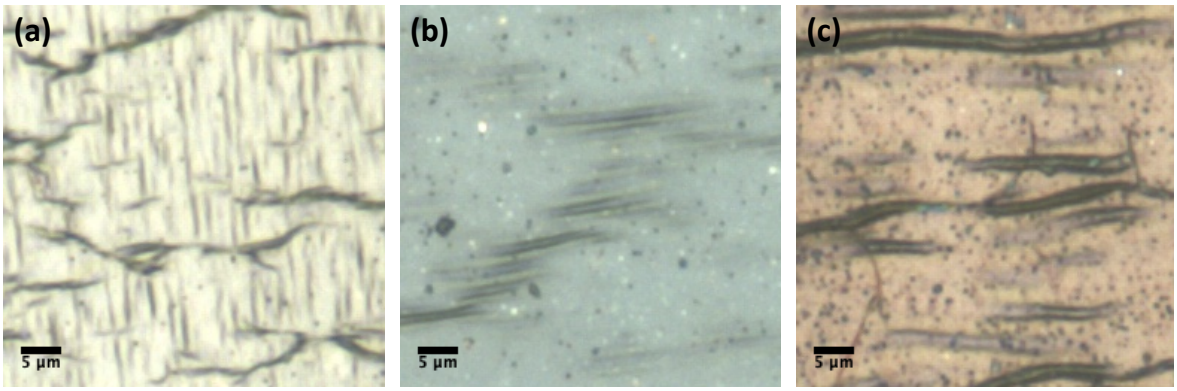

Figure 5.6. Pure SWCNT (a). Pure PEDOT:PSS (b). SWCNT-PEDOT:PSS bilayers (c) of the 40 nm experiment during the 2nd strain cycle at 2% tensile strain in the horizontal direction.

To further enhance the mechanical properties of the SWCNT films, we need to optimize the interfacial width by enhancing the compatibility between the two phases. Here, we demonstrated that the PEDOT:PSS enhanced the mechanical properties of SWCNT without introducing ionic bonding, which requires chemical treatment to the films [25]. In addition, SWCNT films protected the PEDOT:SS film from structural damage a simple way and without any physical or chemical treatments. Some of these treatments might prevent the PEDOT:PSS films from being used in certain applications such as organic light emitting diode where the active layer could be harmed [38].

5.4. Conclusion

In conclusion, we have used the wrinkling approach to investigate the mechanical properties of nanocomposite films consisting of SWCNT-PEDOT:PSS multilayers. We have studied the durability and rigidity of PEDOT:PSS films sandwiched between two SWCNT films. Among the three nanocomposites films, the 20 nm layers showed the most durable behavior, which we attribute to the penetration of PEDOT:PSS into the porous structure of the SWCNT network. The strain softening in the 20 nm and 40 nm experiments was reduced with an increase in the number of layers. However, the 10 nm trilayer showed strain softening. Significant fluctuations in thickness strongly coupled to the rigidity of the layers and decreased the performance of the films with 10 nm layer thickness. In addition, the modulus of PEDOT:PSS dropped with decreasing film thickness due to the reduction of crystalline structure in the PEDOT:PSS. Our results suggest that the rigidity and durability of SWCNT-PEDOT:PSS multilayer films can be enhanced for flexible electronics applications by focusing on film thicknesses that are comparable to the interfacial length scale between the two layers.

6. ENHANCING THE ELASTICITY OF ULTRATHIN SWCNT FILMS WITH COLLODIAL NANOCRYSTALS

6.1. Introduction

Thin films and coatings are present in everyday life, from consumer products to electronic devices. For most applications, fluid-based assembly techniques are beneficial for their ease and scalability, while the rigidity and durability of the thin films are critical to their performance. For some applications, such as touch-screen displays, solar cells, and light-emitting diodes, the electrical characteristics of the film are critical. Within the rapidly evolving field of nanomaterials, single-wall carbon nanotubes continue to show considerable promise and potential for a wide range of applications. Their high Young's modulus (1.2 TPa) makes them suitable for nanocomposite applications, although their full mechanical potential has not yet been realized. SWCNT thin film adhered to a soft substrate and compressed show plastic change (strain softening) in some instances even under small strain. This is because of bundling between SWCNTs mediated by van der Walls interactions between individual SWCNT, which is also associated with small diameter, long length, and high aspect ratio [26].

Recently, the mesoscopic distinct element method (mDEM) was used to explore an excluded-volume approach to stabilizing SWCNT networks against strain-induced plastic change. The main motivation for this hypothesis was reducing the rearrangement of the SWCNT network in response to an applied strain by filling the porous structure with a second nanomaterial, specifically colloidal nanocrystals (NCs) [26,75].

In our work, the wrinkling approach was used to experimentally test the effectiveness of the excluded volume method. Adhered hybrid SWCNT-NC bilayer films on a soft elastic polymer substrate have shown a nearly two-fold enhancement in the Young's modulus. This

enhancement was associated with a thin monolayer of NCs interpenetrating the SWCNT network and preventing the SWCNTs from restructuring in response to the applied strain. The results suggest potential routes to durable hybrid multifunctional nanocomposites films [26].

6.2. Materials and Methods

The experimental procedure was described in section 3.1.3 and Figure 3.6.

6.3. Results and Discussion

The wrinkling approach was used (described in section 3.2.1) to query the film mechanics. The question of whether or not there was an enhancement in modulus associated with the NC monolayer thus came down to a precise knowledge of how much the nanocrystals increased the total thickness of the bilayer. To answer this, we utilized a combination of in situ PL spectroscopy/microscopy and in situ AFM, as shown in Figure 6.1b-c. There is an AFM step-height associated with a small jump in thickness at such an interface, with an overall average value of Δh = (2.65 ± 0.25) nm indicated in Figure 6.1d [26].

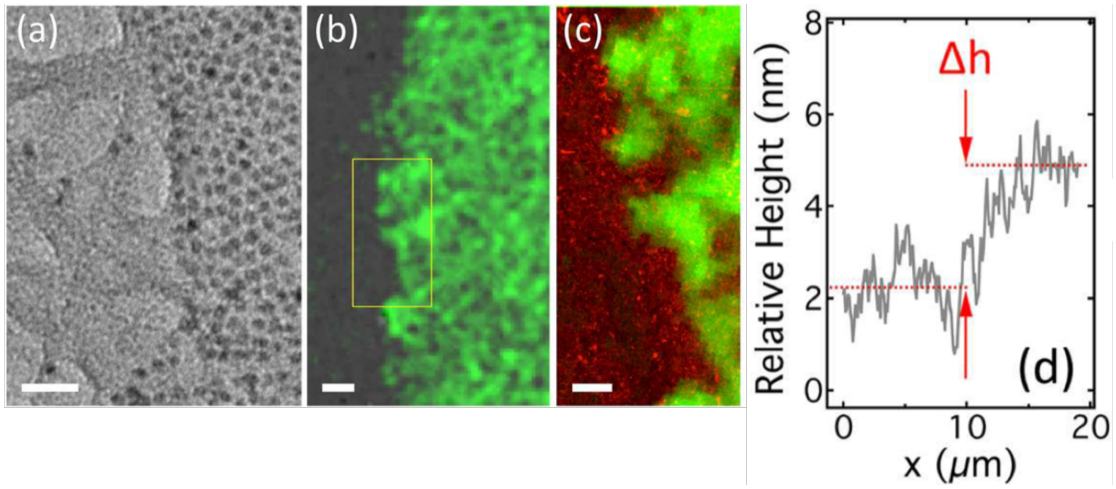

Figure 6.1. TEM image of a SWCNT-SWCNT/NC bilayer interface (20 nm scale) (a). PL image of the bilayer edge over an underlying SWCNT film (10 μm scale) (b). Overlay of PL and AFM images for the region indicated by the yellow rectangle (5 μm scale) (c). Mean step height from SWCNT to NC based on the AFM data (d). Reprinted with permission from Ref. [26]. Copyright 2019 American Chemical Society.

A significant change in wrinkling behavior associated with the presence of a CdSe NC monolayer was clearly evident in composite reflection/PL optical micrographs (Figure 6.2) and in situ AFM measurements of the wrinkling amplitude at the same type of SWCNT−SWCNT/NC interface [26].

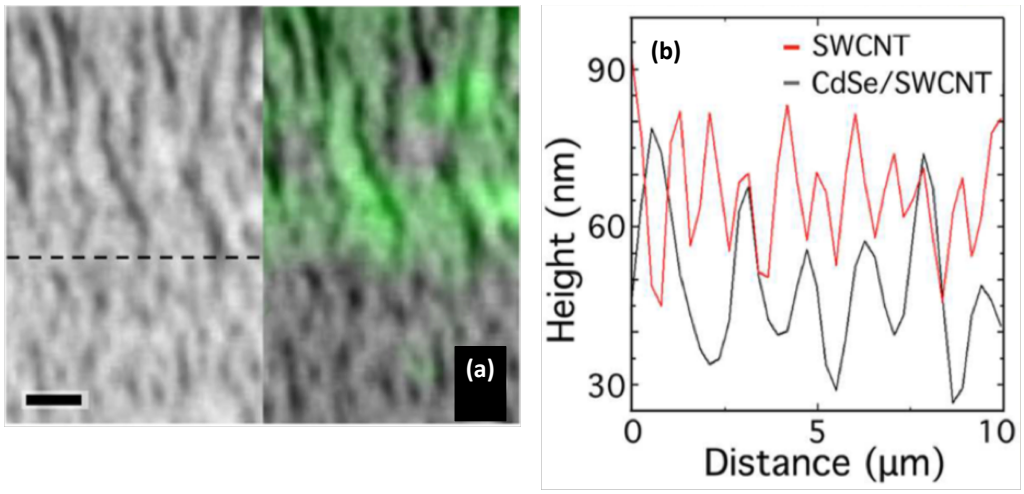

Figure 6.2. Reflection optical micrograph of wrinkling at a NC film edge (h = 21 nm, 10% strain, 5 μm scale) where the right panel is a composite PL image of the same spot (3 μm scale, NC = green) (a). Measured wrinkling amplitude measured with AFM on either side of the bilayer edge (h = 40 nm, 10% strain) (b). Reprinted with permission from Ref. [26]. Copyright 2019 American Chemical Society.

Accounting for the measured Δh, Figure 6.3a-c shows the strain-dependent Young's modulus, both with and without the NC-capping layer, for three SWCNT films over varied thicknesses. For the thinner SWCNT films, the Young's modulus in the presence of the NC monolayer exhibited almost a factor of two enhancement, while the thicker film still suggested somewhat of an improvement in yield strain (Figure 6.3a) [26].

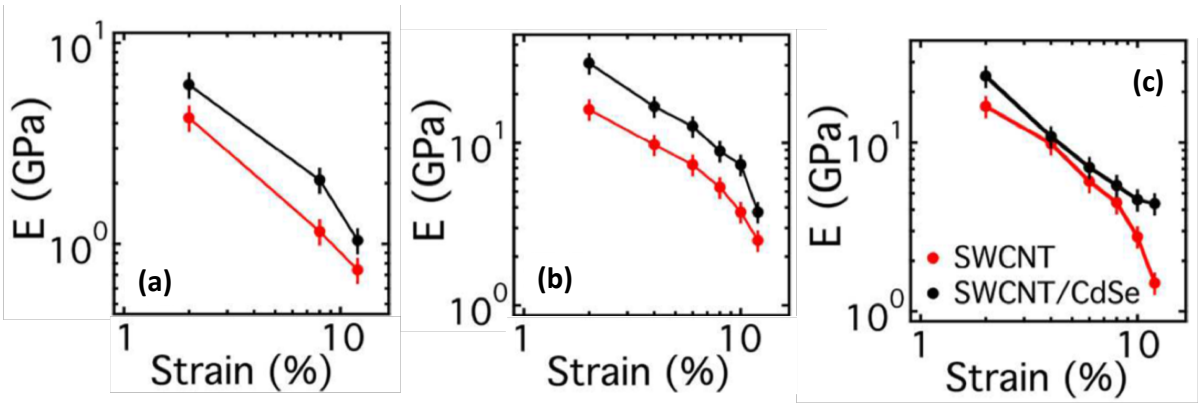

Figure 6.3. Young's modulus of SWCNT and SWCNT/NC for SWCNT film thicknesses of 13 nm (a), 17 nm (b), 40 nm (c). Reprinted with permission from Ref. [26]. Copyright 2019 American Chemical Society.

Filling the porous structure of a SWCNT network with second nanomaterial prevented the nanotubes from restructuring in response to the applied strain. In Figure 6.4a-b, it is apparent that the T1 and T2 SWCNT networks filled with NCs obtained by mDEM simulations are stiffer than pure networks [9,15]. The Young's modulus of a network with 2000 NCs was 9.7 GPa while the pristine network was 7.2 GPa, at 1% tensile strain. These findings are similar to our experimental results for the thinnest SWCNT films coated with NCs [26,75].

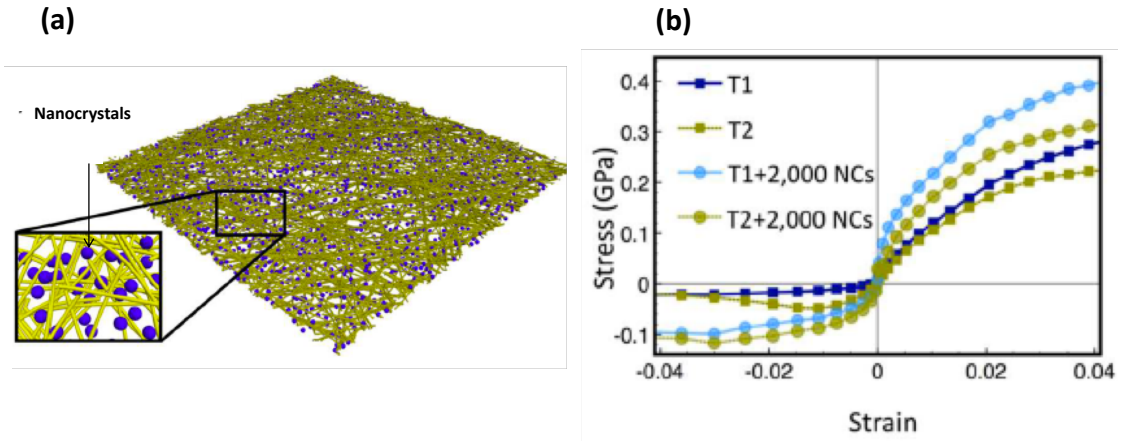

Figure 6.4. Schematic of a SWCNT network filled with NCs (a). Stress-strain curve of SWCNT (T1, T2) and SWCNT/NCs (T1 and T2 with 2000 NCs) based on mDEM simulations (b). Reprinted with permission from Ref. [26]. Copyright 2019 American Chemical Society.

6.4. Conclusion

In conclusion, the wrinkling approach was used to experimentally test the mechanics of hybrid, structured nanotube/nanocrystal bilayers subjected to compressive strain on pre-stretched elastic PDMS substrate. Our measurements indicated a nearly two-fold enhancement in the Young's modulus of ultra-thin films associated with the presence of a monolayer of nanocrystals. These findings are in agreement with mDEM simulations demonstrating an elastic enhancement for thin SWCNT networks filled with NCs. Physically, this is due to the second nanomaterial filling the porous structure of the SWCNT thin film, which reduced the SWCNTs ability to rearrange in response to the applied strain [26,75].

7. DURABLE TRANSPARENT SWCNT/SiNC BILAYER FILMS

7.1. Introduction

Electronic technology is moving toward flexibility and durability. To accelerate this development, it is necessary to have materials with outstanding related properties. Since their discovery, single wall carbon nanotubes have received attention because of their unique one dimensionality. Additionally, they have a high aspect ratio, and 1.2 TPa Young's modulus. The ability of SWCNTs to conduct electricity also makes them attractive for applications in electronic materials. SWCNTs can be either conducting or semi-conducting depending on their molecular symmetry. These properties make SWCNTs ideal for optoelectronic applications, while the sheet-like morphology of SWCNT films is beneficial for many other applications such as touch screens and solar cells that require large contact area [25-27].

However, SWCNT films can suffer from plasticity when they are subjected to applied strain. Previously, we investigated porous structures of SWCNT networks filled with a second material such as CdSe NCs. In that work, we found a significant enhancement in the film elasticity when the porous structures were filled by a second nanomaterial. The second nanomaterial (NC) increased the mechanical stability of the network by filling the gap between the SWCNTs. Moreover, nanocrystals are the best choice to enhance the elasticity of SWCNT films due to a large surface to volume ratio [26].

The combination of SWCNT with other inorganic nanomaterials is a thus a promising approach. Among semiconductor nanoparticles, silicon nanocrystals (SiNCs) have received recent interest due to their low toxicity. Unlike bulk Si, SiNCs have shown photoluminescent properties at different wavelengths depending on their size. SWCNT/NC nanocomposites might replace fragile electrodes and enhance solar cell performance [79-80]. However, a full

understanding of SWCNT-SiNC interactions is rather limited, and considerable effort will be required to take SWCNT-SiNC nanocomposites to the industrial level.

In this work, we have investigated the mechanical properties of ultrathin SWCNT films decorated with SiNCs. Specifically, we have utilized the wrinkling approach to extract the Young's modulus of SWCNT films coated with a thin layer of SiNCs. Using a spray coating method to deposit the SiNCs on SWCNT films, we found a nearly two-fold enhancement in the Young's modulus for ultrathin SWCNT films, while thicker film (~50 nm) suggested a reduction in strain softening. As in previous sections, we attribute the enhancement of the ultrathin SWCNT film elasticity to excluded volume effects, where SiNCs prevented the SWCNTs from aggregating in response to strain. Our results suggest an easy and controllable way to synthesize durable nanocomposites films for multifunctional applications.

7.2. Materials and Methods

The experimental procedure was described in section 3.1.4.

7.3. Results and Discussion

We have utilized the spray coating method to deposit SiNCs on top of SWCNT films partially covered by a Kapton mask. As a result, a sharp interface exists between pristine SWCNT and SWCNT/SiNC bilayer. Additionally, we have used SIEBIMM (as covered in section 3.2.1) to query the mechanics of such thin films adhered to elastic substrates. The changes in wrinkling behavior observed between SWCNT and SWCNT/NC bilayer provide information about the material's response to an applied strain. The other important factor here is how much the SiNC monolayer increases the total thickness of a SWCNT/SiNC bilayer. To address this, atomic force microscopy (AFM) was used to measure the monolayer thickness in situ. Figure 7.1a shows a schematic diagram of the spray coating method of creating

SWCNT/SiNC bilayers. We have kept the same distance (12 cm) between the spray gun and the SWCNT film for all experiments. At fixed SiNC concentration and SiNC flow rate, we tested different distances and found that dewetting occurs below 12 cm, with small circles of SiNC droplets instead of a continuous layer. On the other hand, a larger separation distance shows discontinuities in the SiNC monolayer with isolated islands.

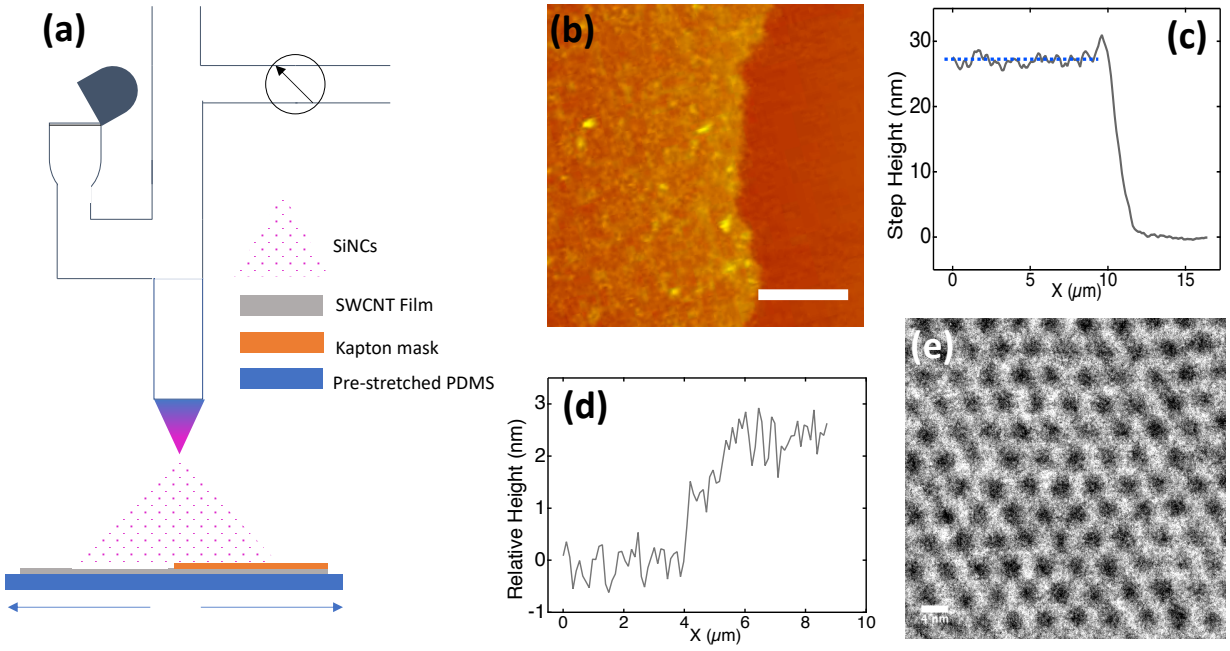

Figure 7.1. Schematic diagram of spray coating SiNCs onto a partially masked SWCNT film (orange color mask) (a). AFM image of a SWCNT film edge (scale bar is 5 μm) (b). Step height of a SWCNT film in (c). Mean step height from SWCNT to SiNC based on AFM (d). TEM image of SiNCs (scale bar is 4 nm) (e).

An AFM height image of a SWCNT film is shown in Figure 7.1b, where the step height of the film is shown in Figure 7.1c. Additionally, Figure 7.1d shows a jump in the NC thickness at such an interface with an overall average of ($\Delta h = 2.50 \pm 0.13$) nm. The TEM image of SiNCs is shown in Figure 7.1e and is associated with a NC size of 3 nm.

We have utilized equation 3.1 to extract the Young's modulus of both pristine SWCNT and SWCNT/SiNC films. It was clear that the distance between each wrinkle in a bilayer was

larger than the pristine SWCNT for a 30 nm SWCNT film, as shown in Figure 7.2a. The wrinkling wavelength of the bilayer was higher than that of the pristine SWCNT ($\lambda_{bilayer} > \lambda_{SWCNTs}$) without a significant change in the total thickness. In addition, the AFM wrinkling amplitude of a SWCNT film and a SWCNT/SiNC bilayer is shown in Figure 7.2b. The AFM amplitude confirmed that the bilayer had fewer wrinkles in comparison to the pristine SWCNT, which at comparable total thickness thus implies a stiffer film.

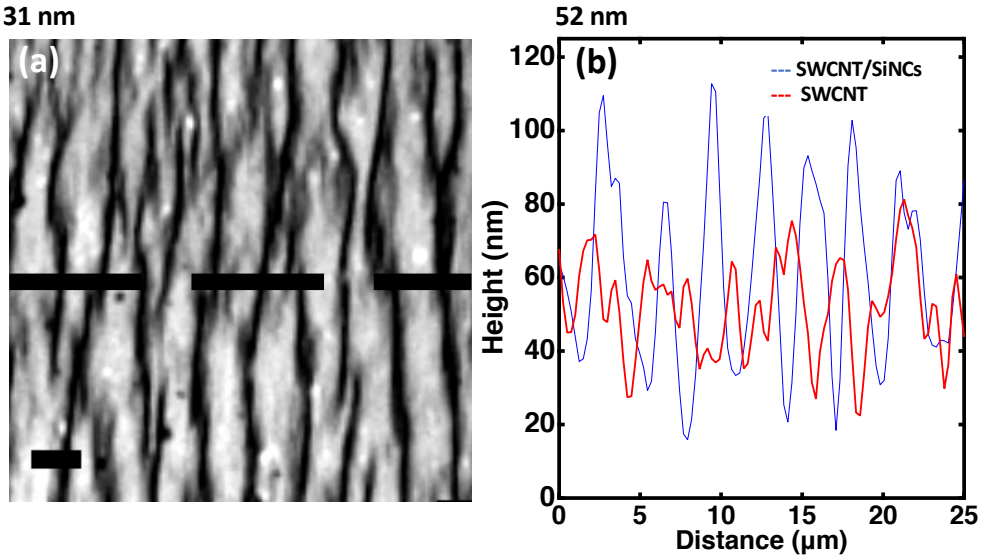

Figure 7.2. Optical reflection image of 32 nm SWCNT-SWCNT/SiNC interface where the interface is indicated by a dashed line (a). AFM wrinkling amplitudes of 52 nm SWCNT and SWCNT-SiNCs bilayer at 10% compressive strain in the horizonal direction (5μm scale) (b).

Accounting for both the buckling wavelength λ and the total film thickness h, the strain dependent modulus is shown in Figure 7.3 for five experiments with different SWCNT film thicknesses. A significant enhancement in film elasticity is apparent for ultrathin SWCNT films coated with SiNCs. The presence of the SiNC layer enhanced the Young's modulus of the SWCNT films up to two-fold.

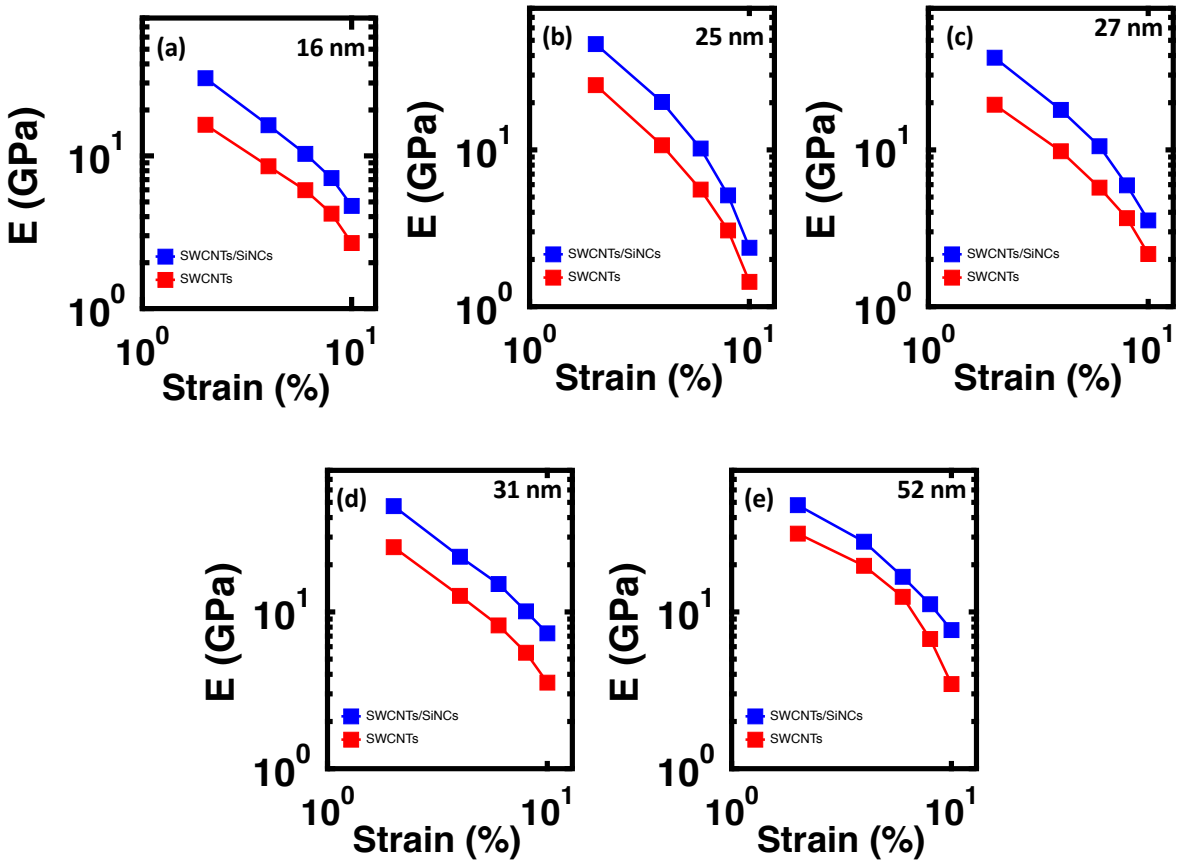

Figure 7.3. Strain dependent modulus of 16 nm (a), 25 nm (b), 27 nm (c), 31 nm (d), and 52 nm (e) SWCNT films with and without SiNC monolayer.

As before, we attribute this enhancement to an excluded volume effect in which SiNCs fill the porous structure of the SWCNT network [26,27]. Previously, we investigated the elasticity of SWCNT films coated with CdSe NCs. There, we found a two-fold enhancement in the Young's modulus of ultrathin SWCNT films coated with CdSe NCs using the Langmuir-Blodgett (LB) method. We attributed this enhancement to the excluded volume effect in the presence of NCs monolayer [26]. In this work, however, we have used a different approach, spray coating, to coat SiNCs on top of SWCNT films. Unlike LB, spray coating provides a larger area of a uniform NC coating. Additionally, time was an issue in the LB method since we had to wait for all solvent to be evaporated. However, spray coating is not suitable for CdSe NCs due to the toxicity of these nanoparticles.

SiNCs have promising applications due to the familiarity of the semiconductor industry with Si-based electronics and these materials have less toxicity in comparison to CdSe NCs. Hybrid SWCNT-SiNC materials represent a promising area of research, especially the combination of different electronic SWCNT types and SiNCs. Understanding these interactions could have potential applications for LEDs and solar cells, for example, where high performance is essential.

7.4. Conclusion

In conclusion, we have utilized a wrinkling approach to understand the mechanics of SWCNT films coated with SiNCs. The SWCNT films were adhered to elastic substrates, where we have used a spray coating method to disperse the SiNCs on top of the SWCNTs. A nearly two-fold enhancement in the elasticity of ultrathin SWCNT films was indicated. We attributed this result to the excluded volume effect of SiNCs on the porous structure of the SWCNT network. Our findings with SiNCs were similar to our previous work, where we found elasticity enhancement in ultrathin SWCNT films coated with CdSe NCs. However, spray coating has the potential to be a faster way to deposit the NCs. In addition, SWCNT-SiNC hybrids are a promising nanocomposites material for many optoelectronic applications such as LEDs and solar cells.

8. OUTLOOK

Colloidal nanomaterials in general are of interest on a number of fronts, particularly in the context of flexible thin films [76-118]. SWCNT films still face some challenges before they can be implemented in flexible electronic devices. Synthesizing and producing SWCNTs remains quite expensive. In addition, there is a potential health concern when it comes to handling SWCNT in a dry state [119]. A full understanding of any potential health issues related to SWCNTs is needed, as well as a reduction in SWCNT production costs.

Aside from the above concerns, SWCNT films can show plastic behavior when strain is applied. This plastic deformation has the potential to limit the application of SWCNT films in flexible electronic devices. Coating SWCNT films with polymers such as passive filler (PS) and active filler (PEDOT:PSS) can reinforce the SWCNT films and reduce strain softening [25]. In this dissertation, we studied the bulk limit of SWCNT-polymer multilayers and found that the films have reached the bulk limit of SWCNT-polymer nanocomposites by six total layers ($n = 6$). In addition, we found significant synergy between SWCNT and polymer occurring for nanocomposites with a common thickness below 30 nm for both active fillers (PEDOT:PSS) and passive fillers (PS) [25]. We attributed the enhancement to the characteristic interfacial width w over which the polymer films penetrate into the porous structure. Further work is needed to understand and optimize the characteristic interfacial width between SWCNTs and polymers where thicker films should be reinforced instead of plasticized [25].

In addition, we have investigated the enhancement of SWCNT films coated with nanocrystals (NCs) by focusing on changes in SWCNT film strain softening. Our goal was to increase film elasticity by reducing the interaction between SWCNT bundles. Specifically, we incorporated both CdSe and Si nanocrystals (NCs). We were able to enhance the film elasticity

by up to a factor of two [26]. We have utilized two different deposition methods to deposit the NCs: Langmuir-Blodgett (LB) and spray coating. We have utilized the LB method to coat SWCNT films with CdSe NCs while a spray-coating method was used to coat SiNCs on SWCNT films. Further work is needed to understand the presence/absence of NCs and how NC concentration, for example, affects the nanocomposite film morphology. The synergy could be further optimized through a design approach based on the relative Hamaker constants of SWCNT-NC interactions and through a more efficient overlay deposition process that optimizes the interpenetration of the NCs into the underlying SWCNT film. For these needs, the soft-stamp approach is a promising transfer method to deposit NC superlattices onto SWCNT films. NCs in a superlattice have the potential for enhanced the electrical properties in SWCNT/NC bilayers if the tunneling resistivity between NCs is reduced. Such an effect would be attributed to the close packing of NCs, which enhances the electron mobility of NC-NC junctions.

Strain-induced elastic buckling instability for mechanical measurements has been utilized here to investigate the mechanics of the nanocomposites. SIEBIMM is a fast and inexpensive tool in comparison to other techniques such as nanoindentation by AFM, an expensive and time-consuming process. However, both SIEBIMM and AFM are destructive methods where the sample will be damaged after testing. Thus, it is necessary to find a new method to query the mechanics of SWCNT films and composites. A macroscopic viscoelastic approach is one promising nondestructive method for studying the mechanics of thin SWCNT films [27]. The van der Waals interactions between the individual SWCNTs can be screened when a SWCNT film suspended in a solvent is deformed and allowed to relax. The relaxation time associated with the film thickness, length, and width can then be used to extract the Young's modulus of the SWCNT film [27].

REFERENCES

1. Buzea, C.; Pacheco, I.; and Robbie K. “Nanomaterials and Nanoparticles: Sources and Toxicity.” *Biointerphases,* **2007,** 2 (4), MR17-MR71.
2. Koo, J. “Fundamentals, Properties, and Applications of Polymer Nanocomposites.” *Cambridge University Press*, **2016,** 273–331.
3. Feynman, R. P. “There's Plenty of Room at the Bottom.” *Engineering and Science*, **1960,** 23, 22-36.
4. Husain, M. and Khan Z. H. “Advances in Nanomaterials.” *Springer: New Delhi, **2016***.
5. Bréchignac, C.; Houdy, P.; and Lahmani, M. “Nanomaterials and Nanochemistry.” *Springer: Berlin,* **2007**.
6. Vollath, D. “Nanomaterials: An Introduction to Synthesis, Properties and Application, 2nd Edition.” *Wiley-VCH: Weinheim,* **2013**.
7. Advani, Suresh G. “Processing and Properties of Nanocomposites.” *World Scientific Pub.*, **2007**.
8. Twardowski, T. E. “Introduction to Nanocomposite Materials: Properties, Processing, Characterization.” *DEStech Publications: Lancaster*, **2007**.
9. Liu, R. “Hybrid Organic/Inorganic Nanocomposites for Photovoltaic Cells.” *Materials,* **2014,** *7*(4), 2747–2771.
10. Zhang, D.; et al. “Transparent, Conductive, and Flexible Carbon Nanotube Films and Their Application in Organic Light-emitting Diodes.” *Nano Letters,* 6.9 **2006,** 1880-1886.
11. Kim, C.L.; Jung, C.W.; and Oh, D.E. “A Highly Flexible Transparent Conductive Electrode Based on Nanomaterials.” *NPG Asia Materials,* 9.10 **2017,** e438.

12. Wright, M. and Ashraf, U. “Organic—Inorganic Hybrid Solar Cells: A Comparative Review.” *Solar Energy Materials and Solar Cells,* 107 **2012,** 87-111.
13. McEvoy, A.; Markvart, T.; and Castaner, L. “Practical Handbook of Photovoltaics: Fundamentals and Applications.” *Elsevier,* **2003**.
14. Knier, Gil. “How Do Photovoltaics Work.” *Science NASA,* **2002**.
15. El Chaar, L. and N. El Zein. “Review of Photovoltaic Technologies.” *Renewable and Sustainable Energy Reviews,* 15.5 **2011**: 2165-2175.
16. Green, Martin A. “Solar Cells: Operating Principles, Technology, and System Applications.” *Englewood Cliffs, NJ, Prentice-Hall, Inc.,* **1982.** 288 p.
17. Horley, P. P.; et al. “Thin Film Solar Cells: Modeling, Obtaining and Applications.” *Application of Solar Energy*. *InTech,* **2013**.
18. Dresselhaus, M. S.; Gene D.; and Peter C. Eklund. “Science of Fullerenes and Carbon Nanotubes: Their Properties and Applications.” *Elsevier,* **1996**.
19. Odom, T. W.; Huang, J.L.; and Charles, M. Lieber. “Single-Walled Carbon Nanotubes.” *Annals of the New York Academy of Sciences,* 960.1 **2002:** 203-215.
20. Anwar, S.; Yasin, M.; Qazi, S.; and Ilyas, M. “Nanotechnology for Telecommunications.” *CRC Press,* **2010**.
21. O’connell, Michael J. “Carbon Nanotubes: Properties and Applications.” *CRC press,* **2006**.
22. Khang, D.Y.; et al. “Molecular Scale Buckling Mechanics in Individual Aligned Single-Wall Carbon Nanotubes on Elastomeric Substrates.” *Nano Letters,* 8.1 **2008:** 124-130.
23. Yu, Min-Feng. “Fundamental Mechanical Properties of Carbon Nanotubes: Current Understanding and the Related Experimental Studies.” *Journal of Engineering Materials and Technology,* 126.3 **2004:** 271-278.

24. Khan, W.; Rahul, S.; and Parveen, S. “Carbon Nanotube-Based Polymer Composites: Synthesis, Properties and Applications. Carbon Nanotubes-Current Progress of their Polymer Composites.” *InTech,* **2016**.

25. Almutairi, E.; Alzaid, M.; Taufique, A.; Semler, M.; and Hobbie, Erik K. “Rigidity of Lamellar Nanosheets.” *Soft Matter,* 13.13 **2017:** 2492-2498.

26. Alzaid, M.; et al. “Enhancing the Elasticity of Ultrathin Single-Wall Carbon Nanotube Films with Colloidal Nanocrystals.” *Langmuir,* 33.32 **2017:** 7889-7895.

27. Alzaid, M.; et al. “Macroscopic Freestanding Nanosheets with Exceptionally High Modulus.” *Langmuir,* 34.27 **2018:** 7951-7957.

28. Semler, M. R.; Harris, J.; and Hobbie, Erik K. “Wrinkling and Folding of Nanotube-Polymer Bilayers.” *The Journal of Chemical Physics,* 141.4 **2014:** 044901.

29. Harris, J.; et al. “Elasticity and Rigidity Percolation in Flexible Carbon Nanotube Films on PDMS Substrates.” *Soft Matter,* 9.48 **2013:** 11568-11575.

30. Xiong, J.; et al. “Liquid Exfoliated Graphene as Dopant for Improving the Thermoelectric Power Factor of Conductive PEDOT:PSS Nanofilm with Hydrazine Treatment.” *ACS Applied Materials & Interfaces,* 7.27 **2015:** 14917-14925.

31. Wang, Y.; et al. “A Highly Stretchable, Transparent, and Conductive Polymer.” *Science Advances,* 3.3 **2017:** e1602076.

32. Worfolk, Brian J.; et al. “Ultrahigh Electrical Conductivity in Solution-Sheared Polymeric Transparent Films.” *Proceedings of the National Academy of Sciences,* 112.46 **2015:** 14138-14143.

33. Shi, H.; et al. “Effective Approaches to Improve the Electrical Conductivity of PEDOT:PSS: a Review.” *Advanced Electronic Materials,* 1.4 **2015:** 1500017.

34. Tahk, D.; Hong, H. L.; and Dahl, K. “Elastic Moduli of Organic Electronic Materials by the Buckling Method.” *Macromolecules,* 42.18 **2009:** 7079-7083.

35. Seitz, J. T. “The Estimation of Mechanical Properties of Polymers from Molecular Structure.” *Journal of Applied Polymer Science,* 49.8 **1993:** 1331-1351.

36. Mermut, O.; et al. “Structural and Mechanical Properties of Polyelectrolyte Multilayer Films Studied by AFM.” *Macromolecules,* 36.23 **2003:** 8819-8824.

37. Lang, U. and Jürg, D. “Mechanical Properties of the Intrinsically Conductive Polymer poly(3, 4-ethylenedioxythiophene)poly(styrenesulfonate) (PEDOT/PSS).” *Key Engineering Materials,* Vol. 345. *Trans Tech Publications*, **2007**.

38. Greco, F.; et al. “Ultra-Thin Conductive Free-Standing PEDOT/PSS Nanofilms.” *Soft Matter,* 7.22 **2011:** 10642-10650.

39. Alex V.; Finkbeiner, S.; and Weber, J. “Temperature Dependence of the Indirect Energy Gap in Crystalline Silicon.” *Journal of Applied Physics,* 79.9 **1996:** 6943-6946.

40. Liu, J.; et al. “Assessing Clinical Prospects of Silicon Quantum Dots: Studies in Mice and Monkeys.” *ACS Nano,* 7.8 **2013:** 7303-7310.

41. Yoffe, Abe D. “Low-Dimensional Systems: Quantum Size Effects and Electronic Properties of Semiconductor Microcrystallites (Zero-Dimensional Systems) and Some Quasi-Two-Dimensional Systems.” *Advances in Physics,* 42.2 **1993:** 173-262.

42. Pucker, G.; Serra, E.; and Jestin, Y. “Silicon Quantum Dots for Photovoltaics: A Review. Quantum Dots-A Variety of New Applications.” *InTech,* **2012**.

43. Sychugov, Ilya. “Synthesis and Properties of Single Luminescent Silicon Quantum Dots.” *Diss. KTH,* **2006**.

44. Huan, C. and Shu-Qing, S. “Silicon nanoparticles: Preparation, properties, and applications.” *Chinese Physics, B*23.8 **2014:** 088102.

45. Mangolini, L.; Thimsen, E.; and Kortshagen, U. “High-Yield Plasma Synthesis of Luminescent Silicon Nanocrystals.” *Nano Letters,* 5.4 **2005:** 655-659.

46. Wang, J.; et al. “Efficient One-Pot Synthesis of Highly Photoluminescent alkyl-functionalised Silicon Nanocrystals.” *Chemical Communications,* 47.17 **2011:** 4941-4943.

47. Basu, S. “Crystalline Silicon–Properties and Uses.” *InTech,* **2011**.

48. Basu, S. and Kanungo, J. “Nanocrystalline Porous Silicon. Crystalline Silicon-Properties and Uses.” *InTech*, **2011**.

49. Wu, C. and Lin, G. “Inhomogeneous linewidth Broadening and Radiative Lifetime Dispersion of Size Dependent Direct Bandgap Radiation in Si Quantum Dot.” *AIP Advances,* 2.4 **2012:** 042162.

50. Miller, J. B.; et al. “Ensemble Brightening and Enhanced Quantum Yield in Size-Purified Silicon Nanocrystals.” *ACS Nano,* 6.8 **2012:** 7389-7396.

51. Svrcek, V.; et al. “A Silicon Nanocrystal/Polymer Nanocomposite as a Down-Conversion Layer in Organic and Hybrid Solar Cells.” *Nanoscale,* 7.27 **2015:** 11566-11574.

52. Nolte, A. J.; Cohen, R. E.; and Rubner, M. F. “A Two-Plate Buckling Technique for Thin Film Modulus Measurements: Applications to Polyelectrolyte Multilayers.” *Macromolecules,* 39.14 **2006:** 4841-4847.

53. Stafford, C. M.; et al. “A Buckling-Based Metrology for Measuring the Elastic Moduli of Polymeric Thin Films.” *Nature Materials,* 3.8 **2004:** 545.

54. Hobbie, Erik K.; et al. “Wrinkling and Strain Softening in Single-Wall Carbon Nanotube Membranes.” *Physical Review Letters,* 104.12 **2010:** 125505.

55. Harris, J. M.; et al. “Electronic Durability of Flexible Transparent Films from Type-Specific Single-Wall Carbon Nanotubes.” *ACS Nano,* 6.1 **2011:** 881-887.

56. Semler, M. R.; et al. “Localization and Length-Scale Doubling in Disordered Films on Soft Substrates.” *Physical Review E,* 88.3 **2013:** 032409.

57. Yu, W. W.; et al. “Experimental Determination of the Extinction Coefficient of CdTe, CdSe, and CdS Nanocrystals.” *Chemistry of Materials,* 15.14 **2003:** 2854-2860.

58. Askeland, D. R. and Wendelin, J. “Science and Engineering of Materials.” *Nelson Education,* **2015**.

59. De, S.; et al. “Transparent, Flexible, and Highly Conductive Thin Films Based on Polymer-Nanotube Composites.” *ACS Nano,* 3.3 **2009:** 714-720.

60. Kim, N.; et al. “Highly Conductive PEDOT: PSS Nanofibrils Induced by Solution-Processed Crystallization.” *Advanced Materials,* 26.14 **2014:** 2268-2272.

61. Gueye, M. N.; et al. “Structure and Dopant Engineering in PEDOT Thin Films: Practical Tools for a Dramatic Conductivity Enhancement.” *Chemistry of Materials,* 28.10 **2016:** 3462-3468.

62. Palumbiny, C. M.; et al. “The Crystallization of PEDOT: PSS Polymeric Electrodes Probed in Situ During Printing.” *Advanced Materials,* 27.22 **2015:** 3391-3397.

63. Jalili, R.; Razal, J. M.; and Wallace, G. G. “Exploiting High Quality PEDOT:PSS–SWNT Composite Formulations for Wet-Spinning Multifunctional Fibers.” *Journal of Materials Chemistry,* 22.48 **2012:** 25174-25182.

64. Araźna, A.; et al. “Modification of Conductive Polymer PEDOT:PSS Layer by SWCNT.” *IOP Conference Series: Materials Science and Engineering*, Vol. 104. No. 1. *IOP Publishing*, **2016**.

65. Tai, Yan-Long and Yang, Zhen-Guo. “Flexible, Transparent, Thickness-Controllable SWCNT/PEDOT:PSS Hybrid Films Based on Coffee-Ring Lithography for Functional Noncontact Sensing Device.” *Langmuir,* 31.48 **2015:** 13257-13264.

66. Lang, U.; Naujoks, N.; and Dual, J. “Mechanical Characterization of PEDOT:PSS Thin Films.” *Synthetic Metals,* 159.5-6 **2009:** 473-479.

67. Fan, X.; et al. “Highly Sensitive, Durable and Stretchable Plastic Strain Sensors Using Sandwich Structures of PEDOT:PSS and An Elastomer.” *Materials Chemistry Frontiers,* 2.2 **2018:** 355-361.

68. Yoo, D.; Kim, J.; and Kim, J. H. “Direct Synthesis of Highly Conductive PEDOT:PSS/graphene Composites and their Applications in Energy Harvesting Systems.” *Nano Research,* 7 **2014:** 717-730.

69. Najeeb, C. K.; et al. “Fabrication of Aligned Ultra-Thin Transparent Conductive Films of Single-Walled Carbon Nanotubes by a Compression/Sliding Method.” *Scripta Materialia,* 64.2 **2011:** 126-129.

70. Zhou, J.; et al. “Semi-metallic, Strong and Stretchable Wet-Spun Conjugated Polymer Microfibers.” *Journal of Materials Chemistry C,* 3.11 **2015:** 2528-2538.

71. Patton, A. J.; Poole-Warren, L. A.; and Green, R. A. “Mechanisms for Imparting Conductivity to Nonconductive Polymeric Biomaterials.” *Macromolecular Bioscience,* 16.8 **2016:** 1103-1121.

72. Zhang, G.; Chu, V.; and Conde, J. P. “Electrostatically Actuated Conducting Polymer Microbridges.” *Journal of Applied Physics,* 101.6 **2007:** 064507.

73. Stafford, C. M.; et al. “Elastic Moduli of Ultrathin Amorphous Polymer Films.” *Macromolecules,* 39.15 **2006:** 5095-5099.

74. Yang, J.; et al. “Stretching-induced Wrinkling in Plastic–Rubber Composites.” *Soft Matter,* 13.4 **2017:** 776-787

75. Wang, Y.; et al. “Excluded Volume Approach for Ultrathin Carbon Nanotube Network Stabilization: A Mesoscopic Distinct Element Method Study.” *ACS Applied Materials & Interfaces,* 9.15 **2017:** 13611-13618.

76. Švrček, V.; Slaoui, A.; and Muller, J-C. “Silicon Nanocrystals as Light Converter for Solar Cells.” *Thin Solid Films,* 451 **2004:** 384-388.

77. Svrcek, V. “Functionalization of Carbon Nanotubes with Luminescent Silicon Nanocrystals upon Nanosecond Laser Processing in Liquid Media.” *Carbon Nanotubes*. *InTech,* **2010**.

78. Švrček, V.; et al. “Connection of Silicon Nanocrystals (Si-nc) with Multi-walled Carbon Nanotubes.” *Applied Physics A,* 83.1 **2006:** 153-157.

79. Svrcek, V.; et al. “Silicon Nanocrystals and Semiconducting Single-walled Carbon Nanotubes Applied to Photovoltaic Cells.” *The Journal of Physical Chemistry Letters,* 2.14 **2011:** 1646-1650.

80. Wong, W. S. and Salleo, A. “Flexible Electronics: Materials and Applications.” Vol. 11. *Springer Science & Business Media*, **2009**.

81. Yuan, H.; et al. “Dispersion Morphology and Correlation to Moduli Using Buckling Metrology in Clay–Biopolymer Nanocomposite Thin Films.” *ACS Applied Materials & Interfaces,* 6.16 **2014:** 13378-13388.

82. Alzoubi, K.; et al. “Comparisons of the Mechanical Behaviors of Poly(3, 4-ethylenedioxythiophene) (PEDOT) and ITO on Flexible Substrates.” *MRS Online Proceedings Library Archive,* 1493 **2013:** 127-132.

83. Mangolini, L.; et al. “Plasma Synthesis and Surface Passivation of Silicon Quantum Dots with Photoluminescence Quantum Yields higher than 60%.” *MRS Online Proceedings Library Archive,* 934 **2006.**

84. Clark, R. J.; et al. “From Hydrogen Silsesquioxane to Functionalized Silicon Nanocrystals.” *Chemistry of Materials,* 29.1 **2016:** 80-89.

85. Miller, J. B.; Harris, J. M.; and Hobbie, Erik K. “Purifying Colloidal Nanoparticles Through Ultracentrifugation with Implications for Interfaces and Materials.” *Langmuir,* 30.27 **2014:** 7936-7946.

86. Van Sickle, A. R.; et al. “Temperature Dependent Photoluminescence of Size-Purified Silicon Nanocrystals.” *ACS Applied Materials & Interfaces,* 5.10 **2013:** 4233-4238.

87. Miller, J. B.; et al. “Enhanced Luminescent Stability Through Particle Interactions in Silicon Nanocrystal Aggregates.” *ACS Nano,* 9.10 **2015:** 9772-9782.

88. Chae, S. H. and Lee, Y. H. “Carbon Nanotubes and Graphene Towards Soft Electronics.” *Nano Convergence,* 1.1 **2014:** 1-26.

89. Ponnamma, D.; et al. “Flexible and Stretchable Electronic Composites.” *Springer*, **2015**.

90. Yamada, T.; et al. “A Stretchable Carbon Nanotube Strain Sensor for Human-Motion Detection.” *Nature Nanotechnology,* 6.5 **2011:** 296-301.

91. Hwang, S.; et al. “Electromechanical Strain Sensing Using Polycarbonate-Impregnated Carbon Nanotube–Graphene Nanoplatelet Hybrid Composite Sheets.” *Composites Science and Technology,* 89 **2013:** 1-9.

92. Torres, J. M.; Stafford, C. M.; and Vogt, B. D. “Impact of Molecular Mass on the Elastic Modulus of Thin Polystyrene Films.” *Polymer,* 51.18 **2010:** 4211-4217.

93. Ding, Y.; et al. “Silicon Nanocrystal Conjugated Polymer Hybrid Solar Cells with Improved Performance.” *Nano Energy,* 9 **2014:** 25-31.

94. Xiong, J.; et al. “Liquid Exfoliated Graphene as Dopant for Improving the Thermoelectric Power Factor of Conductive PEDOT:PSS Nanofilm with Hydrazine Treatment.” *ACS Applied Materials & Interfaces,* 7.27 **2015:** 14917-14925.

95. Dimitriev, O. P.; et al. “PEDOT:PSS Films—Effect of Organic Solvent Additives and Annealing on the Film Conductivity.” *Synthetic Metals,* 159.21 **2009:** 2237-2239.

96. Sun, K.; et al. “Review on Application of PEDOTs and PEDOT:PSS in Energy Conversion and Storage Devices.” *Journal of Materials Science: Materials in Electronics,* 26.7 **2015:** 4438-4462.

97. Harris, J. M.; et al. “Structural Stability of Transparent Conducting Films Assembled from Length Purified Single-Wall Carbon Nanotubes.” *The Journal of Physical Chemistry, C*115.10 **2011:** 3973-3981.

98. Subramani, T.; et al. “High-Efficiency Silicon Hybrid Solar Cells Employing Nanocrystalline Si Quantum Dots and Si Nanotips for Energy Management.” *Nano Energy,* 35 **2017:** 154-160.

99. Träger, F. E. “Springer Handbook of Lasers and Optics.” *Springer Science & Business Media,* **2012**.

100. Obayes, H. R.; et al. “Thermodynamic and Theoretical Study of the Preparation of New Buckyballs from Corannulene, Coronene, and Circulene.” *Journal of Nanomaterials,* **2013:** 1.

101. Sarkar, B.; Satapathy, D. K.; and Jaiswal, M. “Wrinkle and Crack-Dependent Charge Transport in a Uniaxially Strained Conducting Polymer Film on a Flexible Substrate.” *Soft Matter,* 13.32 **2017**: 5437-5444.

102. Fagan, Jeffrey A.; et al. “Comparative Measures of Single-Wall Carbon Nanotube Dispersion.” *The Journal of Physical Chemistry B* 110.47 **2006:** 23801-23805.

103. Fagan, Jeffrey A.; et al. “Centrifugal Length Separation of Carbon Nanotubes.” *Langmuir* 24.24 **2008:** 13880-13889.

104. Rahatekar, Sameer S.; et al. “Length-Dependent Mechanics of Carbon-Nanotube Networks.” *Advanced Materials* 21.8 **2009:** 874-878.

105. Hobbie, Erik K.; et al. “Microscale Polymer−Nanotube Composites.” *ACS Applied Materials &Interfaces* 1.7 **2009:** 1561-1566.

106. Fagan, Jeffrey A.; et al. “Carbon Nanotubes: Measuring Dispersion and Length.” *Advanced Materials* 23.3 **2011:** 338-348.

107. Hobbie, Erik K.; et al. “Empirical Evaluation of Attractive van der Waals Potentials for Type-Purified Single-Walled Carbon Nanotubes." *Physical Review B* 85.24 **2012:** 245439

108. Miller, Joseph B. and Hobbie, Erik K.. “Nanoparticles as Macromolecules.” *Journal of Polymer Science Part B: Polymer Physics* 51.16 **2013:** 1195-1208.

109. Wang, Yuezhou; et al. “Rings and Rackets from Single-Wall Carbon Nanotubes: Manifestations of Mesoscale Mechanics.” *Soft Matter* 10.43 **2014:** 8635-8640.

110. Harris, John M.; et al. “Nature of Record Efficiency Fluid-Processed Nanotube–Silicon Heterojunctions.” *The Journal of Physical Chemistry C* 119.19 **2015:** 10295-10303.

111. Lesyuk, Rostyslav; et al. “Toward Cadmium-Free Spectral Down-Shifting Converters for Photovoltaic Applications.” *Solar Energy Materials and Solar Cells* 151 **2016:** 52-59

112. Harris, John M.; et al. “Impact of SWCNT Processing on Nanotube-Silicon Heterojunctions.” *Nanoscale* 8.15 **2016:** 7969-7977.

113. Brown, Samuel L.; et al. “Enhancing Silicon Nanocrystal Photoluminescence through Temperature and Microstructure.” *The Journal of Physical Chemistry C* 120.33 **2016:** 18909-18916.

114. Elbaradei, Ahmed; et al. “Interaction of Polymer-Coated Silicon Nanocrystals with Lipid Bilayers and Surfactant Interfaces.” *Physical Review E* 94.4 **2016:** 042804.

115. Brown, Samuel L.; et al. “Abrupt Size Partitioning of Multimodal Photoluminescence Relaxation in Monodisperse Silicon Nanocrystals.” *ACS Nano* 11.2 **2017:** 1597-1603.

116. Brown, Samuel L.; et al. “Origin of Stretched-Exponential Photoluminescence Relaxation in Size-Separated Silicon Nanocrystals.” *AIP Advances* 7.5 **2017:** 055314.

117. Brown, Samuel L.; et al. “First-Principles Study of Fluorescence in Silver Nanoclusters.” *The Journal of Physical Chemistry C* 121.43 **2017:** 23875-23885.

118. Brown, Samuel L.; et al. “Superlattice Formation in Colloidal Nanocrystal Suspensions: Hard-Sphere Freezing and Depletion Effects.” *Physical Review E* 98.6 **2018:** 062616.

119. Das, Rasel; Leo, Bey F.; and Murphy, Finbarr. “The Toxic Truth About Carbon Nanotubes in Water Purification: a Perspective View.” *Nanoscale Research Letters* 13.1 **2018:** 183.

APPENDIX. FILMS THICKNESS VALUES

Table A1. Actual thicknesses of SWCNT-PS films. Odd n is SWCNT films while even n is PS thin films [25].

n	10 nm Experiment	20 nm Experiment	40 nm Experiment
1	14.6 (nm)	20.5 (nm)	40.3 (nm)
2	10 (nm)	20.6 (nm)	42.3 (nm)
3	11 (nm)	18.4 (nm)	40 (nm)
4	10.4 (nm)	18.7 (nm)	41.6 (nm)
5	14.4 (nm)	19.8 (nm)	41.3 (nm)
6	11 (nm)	21.5 (nm)	40.8 (nm)

Table A2. Actual thicknesses of SWCNT-PEDOT:PSS films. Layers (*n*) 1 and 3 are SWCNT films while *n* = 2 is PEDOT:PSS. Pristine PEDOT:PSS films are included (last row).

n	10 nm Experiment	20 nm Experiment	40 nm Experiment
1	12.88 (nm)	17.88 (nm)	41.45 (nm)
2	12.53 (nm)	20.05 (nm)	39.43 (nm)
3	14.63 (nm)	19.93 (nm)	39.03 (nm)
PEDOT:PSS	10.72 (nm)	20.16 (nm)	42.32 (nm)

Table A3. Actual thicknesses of SWCNT-CdSe NCs bilayers. The 1st row is pristine SWCNT and the 2nd row is SWCNT/NC bilayer.

Layer	10 nm experiment	17 nm experiment	40 nm experiment
SWCNT	12.72 (nm)	15.70 (nm)	38.68 (nm)
SWCNT/NCs	13.30 (nm)	18.79 (nm)	40.40 (nm)

Table A4. Actual thicknesses of SWCNT-SiNC bilayers. The 1st row is pristine SWCNT films and the 2nd row is SWCNT/NC bilayer.

Layer	15 nm	25 nm	27 nm	30 nm	50 nm
SWCNT	13.43 (nm)	25.71 (nm)	27.56 (nm)	31.50 (nm)	52.50 (nm)
SWCNT/NCs	16.16 (nm)	24.86 (nm)	28.71 (nm)	32.01 (nm)	53.21 (nm)